SLAC-PUB-7848
June 1998

# Switched Matrix Accelerator

David H. Whittum and Sami G. Tantawi
*Stanford Linear Accelerator Center, Stanford CA 94309*

We describe a new concept for a microwave circuit functioning as a charged-particle accelerator at mm-wavelengths, permitting an accelerating gradient higher than conventional passive circuits can withstand consistent with cyclic fatigue. The device provides acceleration for multiple bunches in parallel channels, and permits a short exposure time for the conducting surface of the accelerating cavities. Our analysis includes scalings based on a smooth transmission line model and a complementary treatment with a coupled-cavity simulation. We provide also an electromagnetic design for the accelerating structure, arriving at rough dimensions for a seven-cell accelerator matched to standard waveguide and suitable for bench tests at low power in air at 91.392 GHz. A critical element in the concept is a fast mm-wave switch suitable for operation at high-power, and we present the considerations for implementation in an H-plane tee. We discuss the use of diamond as the photoconductor switch medium.

*Submitted to Review of Scientific Instruments.*

Work was supported by U.S. Department of Energy, Contract DE-AC03-76SF00515.

# Switched Matrix Accelerator

David H. Whittum and Sami G. Tantawi

*Stanford Linear Accelerator Center, Stanford CA 94309*

We describe a new concept for a microwave circuit functioning as a charged-particle accelerator at mm-wavelengths, permitting an accelerating gradient higher than conventional passive circuits can withstand consistent with cyclic fatigue. The device provides acceleration for multiple bunches in parallel channels, and permits a short exposure time for the conducting surface of the accelerating cavities. Our analysis includes scalings based on a smooth transmission line model and a complementary treatment with a coupled-cavity simulation. We provide also an electromagnetic design for the accelerating structure, arriving at rough dimensions for a seven-cell accelerator matched to standard waveguide and suitable for bench tests at low power in air at 91.392 GHz. A critical element in the concept is a fast mm-wave switch suitable for operation at high-power, and we present the considerations for implementation in an H-plane tee. We discuss the use of diamond as the photoconductor switch medium.

*PACS: 29.17+w, 07.57.Yb, 84.40.De, 72.40+w*

## I. INTRODUCTION

The principal instrument for high-energy physics exploration is the microwave accelerator, employed to produce charged particle beams at high center of mass energy.[1] The energy frontier today lies in the range of 0.5 TeV and beyond,[2] and the concept for an accelerator operating there has been the subject of long discussion.[3] Beyond about 5 TeV the received ideas for accelerators correspond to machines of great size, probably larger than society would care to support. In the machine concept known as the linear collider,[4] this size results from the limits on the electric field achievable in a pulsed microwave circuit, due to field-emission and breakdown,[5] and cyclic fatigue due to Ohmic losses in the copper structure.[6] Efficiency also favors low field. These limitations of copper at high-field have motivated a decade of intensive research in other accelerator concepts, primarily

plasma-accelerators.[7] Thus while the high-gradient machine is the focus of advanced accelerator research today, and the ultimate limit for the exploration of physics at the smallest scale, researchers have for the most part abandoned the microwave circuit as a workable concept beyond a gradient in the range of 0.2 GeV/m. In this paper we revisit the problem of acceleration in a conducting structure and describe a new concept operating at mm-wavelengths that may permit gradients beyond 1 GeV/m, on nanosecond time-scales.

Conventional accelerating structures are passive devices, achieving large fields by means of resonant external excitation, over a time scale of order the natural decrement time for fields due to wall losses.[8] For high-energy applications fields must be maintained for several decrement times to permit acceleration of multiple particle bunches. During the time in which the conductor is exposed to electromagnetic fields, Ohmic wall heating within the pulse duration will cause the wall temperature to rise in proportion to the dissipated Poynting flux and the square root of the exposure time.[6] This pulsed temperature variation produces cyclic stress on the conducting material, and limits the gradient at which the structure may be operated. In this work we describe an accelerator concept that permits a much higher gradient, while still employing resonant energy storage and providing acceleration for multiple bunches. The concept is sufficiently far from the conventional that we devote some space in this introduction to sketch the reasoning leading up to it.

In Fig. 1 one sees a charge propagating through a linear array of resonant cavities. These hole-coupled cavities serve a combined function as a transmission line and an accelerator.[9] The circuit equivalent of such a resonant chain invokes an impedance transformation from the low-impedance of the connecting waveguide used to deliver power to the structure, to the high shunt impedance of the resonant cavities. The time-domain analog of this impedance transformation is the resonant filling of a cavity, the excitation over many cycles of an electric displacement in the cavities that is much larger than the externally provided electric field in the waveguide. Hole-coupling along the beam axis permits a single waveguide feed once every $10^2$ periods, and a corresponding increase in the equivalent impedance. The technology employed in Fig. 1 has been developed over the course of some fifty years, commencing with the cavity concepts of Hansen,[10] and evolving into machines of 100 m scale,[11] and later 3 km scale.[12] The engineering design for a 30 km machine is under discussion.[13]

For efficient use of resonant enhancement, the fill-time of the structure should be of order the natural decrement time of the fields due to Ohmic losses, about $10^{-6}$ s at S-Band (2-4 GHz), and $10^{-8}$ s at W-Band (75-110 GHz). In this amount of time, and in a cavity volume of small size optimized for a large accelerating electric field, the wall temperature will rise in proportion to the squared gradient, approaching the cyclic stress limit for copper at 0.25 GeV/m.[6] Beyond 1 GeV/m, the temperature rise in a travelling-wave structure would exceed 700 K, enough to ablate the copper surface in a single pulse and detune the cavity from synchronism, quickly rendering it useless. This is the dilemma we wish to overcome.

We are lead then to contemplate revisions to the accelerator concept, as illustrated in Fig. 2. In Fig. 2(a) we see again the conventional concept, and in Figs. 2 (b) and (c), two naive notions for avoiding pulsed heating. In Fig. 2(b), we imagine a shorter electromagnetic pulse, and a shorter structure. Realizing that in such a structure the gradient is not maintained long enough to accelerate the multiple bunches required for a collider, and realizing also that too much power would be dumped unused in the load, we suppose that parallel structures are employed, with a cascading of feeds. In Fig. 2(c), we carry this idea of cascading to the extreme, and contemplate a matrix of cells, and signal transmission along an axis independent of the beam direction. These cartoon concepts illustrated in Figs. 2(b) and 2(c) present, on second thought, some difficulties. The power distribution requires numerous feeds, and implies either equally numerous sources, each providing a very short pulse, or a means of multiplexing and delaying high-power signals from a single source to place them in the correct schedule for acceleration.

Considering in more detail how acceleration is to be accomplished in the scheme of Fig. 2 (c), we sketch the layout of Fig. 3, and observe two additional problems. First, the smooth waveguide illustrated there exhibits no resonant enhancement, *i.e.*, the impedance is low, and thus the peak power required would be exorbitant. Not surprisingly, then, we will need to design a *loaded* transmission line and characterize the efficacy of its component cavities. A second, subtler concern is that orthogonal propagation of the signal and the beam may result in a *transverse* kick imparted to the beam. A transverse kick is undesirable in an accelerator, as high energy particles radiate copiously when deflected, and are subject to transverse collective instabilities that could be seeded by such kicks. This is

primarily a beam dynamics problem and, while its solution may ultimately impose requirements on the electromagnetic design, we will address it summarily here. A transverse kick may be compensated in one of three ways: by an external magnetic field, by special purpose cavities designed to provide a compensating kick, or by permitting a deviation from orthogonality between the beam-axis and the signal propagation axis. We will put aside this last complicating feature for a later work as it does not significantly effect the scalings or the circuit performance of the device, the subject of this work.

In this work we will devise an electromagnetic circuit that addresses the problems associated with the concept of Fig. 2(c) and Fig. 3, permitting a reasonable number of feeds, as well as resonant field enhancement. This circuit will permit efficient multibunch acceleration, with a short exposure time for the accelerating structure. When complete we will have arrived at the signal and bunch schedules illustrated in Fig. 4, and contrasted there with the conventional schedules. We will not attempt here to solve all of the research questions posed by the concept illustrated in Fig. 4; instead we will consider only the essential features of its operation as a microwave circuit and an accelerator. Thus fundamental mode deflections and higher mode wakefields will not be studied. The concept is amenable to a number of different techniques for delivery of power to the accelerating structure, including so-called two beam accelerator techniques.[14] Here we will consider its implementation in the abstract, from the power feed to the load, independent of the method of power generation.

In Sec. II we outline the concept and the macroscopic circuit parameters characterizing its performance. We analyze in detail the transient features of the device that are fundamental to its operation. In Sec. III we provide an illustrative example for operation at W-Band, accompanied with circuit simulations. In Sec. IV we provide an example electromagnetic design for one accelerating cell, and for a 7-cell test-block matched to standard waveguide. The concept requires a fast microwave switch, and in Sec. V considerations for such a switch are set down, informed by previous studies of high-power switches at X-Band, and experience with diamond as a photoconductor. Both the switch and the 7-cell test block are stand-alone two-port microwave elements mated to standard waveguide, and thus suitable for bench studies. Finally, in Sec. VI, we offer conclusions and discuss areas for future work.

Numerical examples will correspond to a switched matrix accelerator at W-Band

(91.392 GHz or "32 x SLAC"), with beam parameters commensurate with the requirements for a 5 TeV collider.[15] The interest in acceleration at W-Band and shorter wavelengths has been discussed at length elsewhere;[6] for purposes of this work, perhaps it is enough to observe that physical space requirements favor such a length scale, or smaller. At W-Band the transverse extent of the accelerator illustrated in Fig. 4 is under 6 inches for 50 parallel beamlines.

## II. CIRCUIT ANALYSIS

The circuit implementation of Fig. 4 is indicated in Figs. 5(a) and (b), and consists of a primary transmission line coupled by means of fast switches to a series of parallel secondary transmission lines. Operation consists of three steps: (1) resonant filling of the primary line with mm-wave power $P_1$, provided by an external power source on the natural field decrement time scale of $10^{-8}$ s (2) rapid closing of the switches on a time scale well under $10^{-9}$ s (3) propagation of a short sub-nanosecond burst of mm-waves down the secondary line, as single electron bunches arrive in parallel, to be accelerated as they pass through each secondary line, roughly orthogonal to the direction of mm-wave propagation. In this section we set down the basic scalings for a particular geometric implementation of such a device.

We implement the circuit of Fig. 5, with the geometry illustrated in Figs. 6 and 7. This single-depth rectangular geometry is chosen to simplify the problem of fabrication on the mm-scale. The primary line could be implemented either as a standing-wave cavity, or an iris-coupled travelling wave structure. The latter has the conceptual virtue of coupling in a transparent manner, after switch closure, where each cell has the appearance of $TE_{10}$ waveguide, iris-coupled into a secondary transmission line consisting of periodically-loaded $TE_{10}$ waveguide. The former has the advantage of lower wall losses, and thus higher efficiency. We view the primary cells during discharge as uncoupled from each other, and strongly coupled (matched) to the corresponding secondary transmission line. For this work we put aside the question of secondary-secondary coupling through the beam ports and assume good isolation has been achieved, for example, by means of a choke feature between adjacent secondary cells.

### *A. Energetics*

The primary line is filled with input power $P_1$, corresponding to steady-state stored energy $U_1$ per primary period $L$. The stored energy density in the primary $u = U_1 / L$ constrains the energy requirements for the linac on a single machine repetition. For simplicity, we will take the cell-length $L$ in the primary to be constant. Synchronism between the signal and the beams imposes a requirement on phase-advance per cell $\theta_1$ in the primary, $\theta_1 = \omega L / c$. Thus constant cell-length and constant phase-advance per cell are equivalent assumptions. One could deviate from this condition at the expense of some additional variety in the interconnect between primary and secondary. In addition, we ask that the stored energy per unit length be constant throughout the primary. For a travelling-wave primary, this implies a tapering of the group velocity to compensate wall-losses, $dV_{g1} / dz = -\omega / Q_{w1}$, with $\omega$ the angular frequency of the signal and $Q_{w1}$ the wall $Q$ of one primary cell. Scalings for such a constant-gradient transmission line are determined by the choice of the initial group velocity; this determines the attenuation parameter

$$\tau_1 = -\frac{1}{2}\ln\left(1 - \frac{\omega N_1 L}{V_{g1}(0) Q_{w1}}\right). \tag{1}$$

with $N_1$ the number of cells in the primary. The fill-time is $T_1 = 2Q_{w1}\tau_1 / \omega$, the steady-state power to the load is $P_1 \exp(-2\tau_1)$, and the stored energy per cell is $U_1 = P_1 L / V_{g1}(0)$. This last relation may also be expressed as a requirement on peak power

$$P_1 = N_1 U_1 \frac{\omega}{Q_{w1}}\left(1 - e^{-2\tau_1}\right)^{-1}. \tag{2}$$

An alternative to a travelling-wave primary line is a standing-wave cavity, obtained by removing the coupling irises in Fig. 7. The advantage of removing the irises is that wall-losses are reduced by about a factor of two. In this case, the energy $U_1$ available for discharge into one secondary line is given by

$$N_1 U_1 = \frac{2\beta}{1+\beta}\frac{\left(1-e^{-\tau_1}\right)^2}{\tau_1}\left(P_1 t\right), \tag{3}$$

where $P_1$ is the incident power, $t$ is the pulse duration, and for the standing-wave implementation we redefine $\tau_1 = t/T_1$ , with $T_1 = 2Q_{w1}/(1+\beta)\omega$, the loaded fill-time. The coupling parameter $\beta = Q_{w1}/Q_{e1}$, with $Q_{e1}$ the external $Q$. Efficiency is a maximum for $\tau_1 \approx 1.26$, and is given by $\eta_1 \approx 0.815\,\beta/(1+\beta)$. For example, $P_1 \approx 2N_1U_1/T_1$ for critical coupling ($\beta = 1$).

After switch closure, each primary cell discharges down the adjacent secondary transmission line. Decomposing the fields in each primary cell into forward and reverse waves propagating in *x,* one can see that the shape of the waveform incident from the primary cell depends on the coupling, approaching an exponential decay in the limit of weak coupling. We will suppose that each cell is well-coupled, so that the primary cell produces a square wave with pulse length $T_p = 2w_1/V_{gp}$, where $V_{gp}$ is the group velocity in the primary cell viewed as rectangular waveguide, and $w_1$ is the length of the primary cell in $x$. The peak power incident on the secondary line may then be expressed as $P_2(x=0) = U_1/T_p$. At any point along the secondary we may relate the power flowing through the line to the group velocity for the secondary $V_{g2}$, and the energy stored in a secondary cell $U_2$ according to $P_2 = V_{g2}U_2/w_2$. For a strictly periodic constant-impedance secondary line, $V_{g2}$ is constant, and $U_2$ and $P_2$ evanesce along the line due to wall-losses. Such attenuation favors consideration of a geometry which has been tapered, decreasing $V_{g2}$ toward the output end in such a way as to cause the emitted waveforms to compress, enhancing the cell voltage. Such a taper, for the case of a transmission line operated in *steady-state,* would be just the constant-gradient taper described above in the discussion of the primary line. In this case, $dV_{g2}/dx = -\omega/Q_{w2}$, and the line would be characterized by attenuation parameter

$$\tau_2 = -\frac{1}{2}\ln\left(1 - \frac{\omega N_2 w_2}{V_{g2}(0)Q_{w2}}\right), \tag{4}$$

with $w_2$ the secondary period, and $N_2$ the number of secondary cells. Ours is not a steady-state problem, however, and additional analysis will be required of the transient features effecting cell voltage. We will find that dispersion places a significant lower-bound on the group velocity, constraining it as a function of $N_2$ and $\omega T_p$.

The no-load gap voltage $V_{NL}$ for a single accelerating cavity containing energy $U_2$ may be expressed as $V_{NL}^2 = \omega U_2 [R/Q]$ where the quantity $[R/Q]$ for one cavity of the secondary line is a single parameter determined by the geometry. The unloaded accelerating gradient can be determined from $G_{NL} = V_{NL}/L$. Phase-advance per cell in the secondary will be determined by the need to minimize dispersion, and thus should be near mid-band, an odd multiple of $\pi/2$. At this point in the analysis we need to contemplate the geometry to understand the circuit parameters actually achievable.

### *B. Geometry*

The geometry is illustrated in Fig. 8. We assume a common depth dimension, *a*, for all cells. In the first approximation, both the primary cell, and the secondary cell are rectangular pillboxes. and we may determine the basic circuit parameters in terms of the fields of a closed pillbox. For a closed pillbox excited in the $\mathrm{TE}_{10\mathrm{m}}$, with resonant angular frequency $\omega_0$, we may express the electric and magnetic fields as

$$\underline{E}(\underline{r},t) = \Re\left\{\tilde{E}(\underline{r})e^{j\omega_0 t}\right\}, \qquad \underline{H}(\underline{r},t) = \Re\left\{\tilde{H}(\underline{r})e^{j\omega_0 t}\right\},$$

where $\tilde{E}$ and $\tilde{H}$ have components

$$\tilde{E}_z = \tilde{E}_0 \sin(\beta_x x)\sin(\beta_y y),$$

$$Z_0\tilde{H}_y = -j\frac{\beta_x}{\beta_0}\tilde{E}_0 \cos(\beta_x x)\sin(\beta_y y), \quad Z_0\tilde{H}_x = j\frac{\beta_y}{\beta_0}\tilde{E}_0 \sin(\beta_x x)\cos(\beta_y y).$$

The free-space impedance is $Z_0 \approx 376.7\,\Omega$, and the wavenumbers are $\beta_y = \pi / a$, $\beta_0 = \omega_0 / c = \sqrt{\beta_y^2 + \beta_x^2}$, with $\beta_x = m\pi / w_1$ for the primary cell, and $\beta_x = \pi / w_2$ for the secondary. We are considering an overmoded primary cell ( $m > 1$), to permit high energy storage at low field, while we consider a fundamental-mode ( $m = 1$) secondary cell, to permit high gradient at low stored energy. The wall *Q* may be computed from

$$\frac{1}{Q_w} = \frac{\delta}{2} \frac{\int_{walls} dS \left|\tilde{H}\right|^2}{\int_{volume} dV \left|\tilde{H}\right|^2} = \frac{R_s}{Z_0} \frac{2}{\beta_0} \left\{ \frac{1}{L} + \frac{2}{w} \frac{\beta_x^2}{\beta_0^2} + \frac{2}{a} \frac{\beta_y^2}{\beta_0^2} \right\}, \tag{5}$$

with $\delta = \sqrt{2 / \mu\sigma\omega}$ the skin-depth and $R_s = 1/\sigma\delta$ the surface resistance. The quantity $w = w_1$ for the primary cell, and $w = w_2$ for the secondary cell.

To compute $[R/Q]$ for the secondary transmission line viewed as an accelerator, we consider the geometry sketched in Fig. 8. An electron passing through the cavity on a ballistic trajectory, parallel to the *z*-axis witnesses the electric field

$$\dot{E} = \hat{z}\, \Re \tilde{E}_0 \sin(\beta_x x) \sin(\beta_y y) e^{j\omega t}. \tag{6}$$

and this may be integrated across the gap to obtain the electron energy change,

$$\Delta\varepsilon = -e \int_0^L dz\; E_z\left(x, y, z, t = t_0 + \frac{z}{c}\right), \tag{7}$$

with *-e* the electron charge and $t_0$ the arrival time at the cavity entrance. This may expressed in terms of an effective cavity voltage phasor, $\tilde{V}_c$, such that on the beam-axis $\Delta\varepsilon = -e\Re\tilde{V}_c e^{j\omega t}$. With this definition, $\tilde{V}_c = \tilde{E}_0 LT \exp(j\theta/2)$, where $\theta = \beta_0 L$ is the transit

angle and $T = \sin\left(\frac{\theta}{2}\right)/\left(\frac{\theta}{2}\right)$ the transit time factor. The energy stored in the cavity may be expressed as $U_2 = V\left|\tilde{E}_0\right|^2 / 8cZ_0$, where $V_2 = aLw_2$ is the secondary-line cavity volume. These results allow us to compute

$$\left[\frac{R}{Q}\right] = \frac{\left|\tilde{V}_c\right|^2}{\omega U_2} = Z_0 \frac{16}{\beta_0^2 a w_2} \frac{\sin^2\left(\frac{\theta}{2}\right)}{\left(\frac{\theta}{2}\right)}. \tag{8}$$

In terms of $[R/Q]$ one may proceed to quantify single-bunch beam-loading with the loss-factor $k_l = \omega[R/Q]/4$. Single-bunch beam-induced voltage is then $V_b \approx -2k_l Q_b$, for a charge $Q_b$.

Next, we assess wall-heating in a single pulse. The time-averaged Poynting flux into the wall, at a location of maximum dissipated power density (a "hot-spot") may, in either cavity, be expressed as

$$S_{\max} = \frac{\omega U}{V} \eta_g \delta, \tag{9}$$

where $V$ is the cavity volume, $V = V_1 = aLw_1$ for the primary, and $V = V_2 = aLw_2$ for the secondary. The factor

$$\eta_g = 2 \times \max\begin{cases} 1 - \frac{\beta_y^2}{\beta_0^2} \\ \frac{\beta_y^2}{\beta_0^2} \end{cases} \tag{10}$$

and $\eta_g \geq 1$, with equality if $w_1 = ma$ (for the primary) or $w_2 = a$ (for the secondary). Temperature variation at a conducting boundary is determined from[6]

$$C\frac{\partial T}{\partial t} \approx \delta(\xi) S_{\max} + \kappa \frac{\partial^2 T}{\partial \xi^2},$$

where $\xi$ is the normal coordinate into the surface, and we consider the limit of diffusion depth long compared to a skin-depth. For room-temperature copper the thermal conductivity is $\kappa = 401\,\mathrm{W/K-m}$, and the volume specific heat capacity is $C = 3.45\times10^{6}\ \mathrm{J/K-m^3}$. We solve Eq. (9) with a Laplace transform in *t*, and boundary conditions corresponding to no heat flow into the vacuum, $\partial T/\partial\xi = 0$ at $\xi = 0$. Two cases are of interest and for either we may express the result for the temperature rise at the surface after time *t* as[16]

$$\Delta T_{\max}(t) = \frac{2S_{\max}}{\sqrt{\pi\kappa C}}t^{1/2}\eta_t, \tag{11}$$

For a *square* waveform $\eta_t = 1$, and this is the case for the first secondary cell, where $t = T_p$ at the end of the pulse. Subsequent cells will see lower pulsed heating due to broadening of the waveform. For the primary cell, the waveform is determined from Eqs. (3) and (9), and has an exponential character. In this case[17]

$$\eta_t = 1 - 2\frac{F\left(\sqrt{\tau_1}\right)}{\sqrt{\tau_1}} + \frac{F\left(\sqrt{2\tau_1}\right)}{\sqrt{2\tau_1}},$$

where *F* is Dawson's integral and $\tau_1 = t/T_1$.[17] So, for example, for $\tau_1 \approx 1.27$, $\eta_t \approx 0.326$, and for $\tau_1 \approx 1.0$, $\eta_t \approx 0.244$. Pulsed-heating is lower than in the secondary, due to the lower peak dissipated Poynting flux and due to the transient character of the waveform.

With these results in hand, let us consider choices of dimensions. Minimum stored energy density on the primary line, $U_1/L$, favors maximum $[R/Q]/L$. This corresponds to maximum transit-angle factor, *i.e.*, small transit-angle. For example, a transit-angle of $\theta \approx 90°$ requires stored energy in the primary line that is half that for $\theta \approx 180°$, and 23% more than for the theoretical limit $\theta \to 0$. However, in practice, for too small a transit angle, the finite width of copper between the secondary lines will reduce the effective

$[R/Q]/L$. In addition, $Q_w$ suffers as transit angle is reduced, approaching 0 in the limit $\theta \to 0$. Since we have put aside, for this work, modelling of the coupling of adjacent secondary lines through the beam tubes, we will optimize instead the stored energy per secondary line. This corresponds to maximizing $[R/Q]$ and occurs for $\theta \approx 133.6°$, $T \approx 0.788$, and $L = 0.371\lambda$ with $\lambda$ the free-space wavelength. Maximum $[R/Q] \approx 221.3\,\Omega$ occurs for $a = w_2 = \lambda/\sqrt{2}$.

At 91.392 GHz the dimensions $a = w_2 = 2.32$ mm, $L = 1.22$ mm. For room-temperature copper $\delta \approx 0.22\mu m \approx 9\ \mu$inch and $R_s \approx 79$ m$\Omega$. In this case $Q_{w2} \approx 2.7 \times 10^3$ assuming a surface roughness much less than $\delta$, and this corresponds to a field decrement time of $2Q_{w2}/\omega \approx 9.4$ ns. For a gradient $G = \left|\tilde{E}_0\right| T \approx 1$ GeV/m, the peak electric field is 1.27 GeV/m, and the cell-voltage is $\left|\tilde{V}_c\right| \approx 1.22$ MeV. Pulsed temperature rise is $\Delta T_{\max} \approx 126$ K, for a square-wave with width $T_p \approx 0.33$ ns. Loss-factor is $k_l \approx 32$ V/pC, and the effect of loading is to place a limit on the charge that can be accelerated. While the behavior of the beam-induced voltage on the transmission line remains to be analyzed, the most conservative estimate would *add* beam-induced voltages. In this case, for example, if we hold net beam-induced voltage on the line to 15% of the no-load voltage, we may accelerate at most 3 nC divided into $N_2$ bunches. This estimate turns out to be too conservative as we will see in Sec. III.

These closed-pillbox estimates provide insights into the scalings and are a useful guide to rough dimensions; however some limitations should be noted. The actual transverse dependence of cavity voltage, with beam tubes, differs from that of a closed pillbox. Electric field lines bend away from the beam axis in the vicinity of the ports and thus without field-shaping features, $[R/Q]$ will be lower than the ideal. In the meantime, gradient may be always be determined according to

$$G^2 = \omega\left(\frac{U_2}{L}\right)\frac{1}{L}\left[\frac{R}{Q}\right], \tag{12}$$

and is always lower than the maximum electric field, due to the transit time effect. In general pulsed temperature rise in the secondary may always be expressed as

$$\Delta T_{\max} \approx \frac{0.837}{\sqrt{\kappa C}}\left(\frac{\delta}{\lambda}\right)\frac{G^2 T_p^{1/2}}{[R/Q]}\eta_g\eta_t, \tag{13}$$

however, the factor $\eta_g$ depends on the actual geometry, and may be larger than the ideal. The factor $\eta_t$ depends on the waveform shape. For the sake of comparison we note that the temperature rise in a conventional accelerator circuit satisfies the same scaling, but requires a longer exposure time. At W-Band, with a fill-time of order 9.4 ns, and the same gradient, the temperature rise would be $660\,\mathrm{K}$. To compare with other choices of wavelength, note that for a conventional travelling-wave linac of fixed geometrical shape, and ideal surface finish, $\Delta T_{\max} \propto \lambda^{1/4}$. Thus in an eight-times larger X-Band accelerator one obtains $1100\,\mathrm{K}$.

Having fixed the depth and width dimensions of the secondary we have constrained the parameters for the primary cell. The group velocity in the primary line, with the switch on, where it can be viewed as a length of straight waveguide, is given by $V_{gp}/c = 1/\sqrt{2}$. The duration of the output pulse is just twice the transit time on this length of line and this is $T_p = 2m/f$, with *f* the signal frequency. Taking account of pulsed heating in the time $T_p$ we will settle on $m \approx 15$. In this overmoded limit the primary wall $Q$ can be rather high, $Q_{w1} \approx 3.57\times10^3$ with a field decrement time $2Q_{w1}/\omega \approx 12.4$ ns ($Q_{w1} \approx 3.65\times10^3$ in the limit of large *m*). Still higher *Q* can be achieved by removing the somewhat artificial iris-loading from the primary, reducing it to a standing-wave structure. In this case the natural period length is adjusted slightly $L = \lambda/2$, and $Q_{w1} \approx 9.94\times10^3$ for $m \approx 15$, with a natural decrement time of $2Q_{w1}/\omega \approx 34.6$ ns at 91.392 GHz ($Q_{w1} \approx 1.06\times10^4$ in the limit of large *m*). With critical coupling, the loaded fill-time for our parameters is then $T_1 \approx 17.3$ ns.

### *C. Dispersion*

Taken together our results thus far provide the basic scalings for the matrix accelerator, except for one feature: dispersion. Our application, unusually, relies on the

propagation of a transient pulse down a line of relatively low group velocity. In this section we quantify how short a pulse we may propagate in a transmission line with low group velocity, while maintaining high cell voltage. There are two features of the problem that bear in our favor. Firstly, a peaking voltage is required in a secondary cell for only a short duration, *i.e.*, we are not interested in filling the entire secondary. Secondly, the dispersion curve for the secondary line may be designed without the usual synchronism constraint that applies to conventional travelling wave structure. We analyze first a uniform transmission line, then a periodic line, and finally a quasi-periodic, tapered line.

We consider a uniform transmission line characterized by a dispersion relation $\beta(\omega)$, specifying wavenumber $\beta$ as a function of angular frequency $\omega$. We suppose that a voltage is specified at the input to the line ($x$=0), as the real part of $V(t,0)=\tilde{V}_0(t)\exp(j\omega_0 t)$. The phasor $\tilde{V}_0(t)$ conveys both amplitude and frequency modulation. In the frequency domain we have,

$$\tilde{V}(\omega,0)=\int_{-\infty}^{\infty}\frac{dt}{\sqrt{2\pi}}\tilde{V}_0(t)e^{j(\omega_0-\omega)t}, \tag{14}$$

and, inverting this expression, we arrive at the voltage at a location *x*,

$$V(t,x)=\int_{-\infty}^{\infty}\frac{d\omega}{\sqrt{2\pi}}\tilde{V}(\omega,0)e^{j\omega t-j\beta(\omega)x}=e^{j\omega_0 t-j\beta(\omega_0)x}\tilde{V}_x(\tau) \tag{15}$$

where

$$\tilde{V}_x=\int_{-\infty}^{\infty}\frac{d\omega_1}{\sqrt{2\pi}}\tilde{V}(\omega_0+\omega_1,0)e^{j\Phi}, \tag{16}$$

the phase in the exponent is

$$\Phi(\omega_1,\tau,x)=\omega_1 t-\left[\beta(\omega)-\beta(\omega_0)\right]x=\omega_1\tau-x\left[\frac{1}{2!}\beta''(\omega_0)\omega_1^2+\frac{1}{3!}\beta'''(\omega_0)\omega_1^3+\mathsf{K}\right], \tag{17}$$

and we introduce the variable, $\tau=t-x\beta'(\omega_0)$.

Our interest is in evaluating $\tilde{V}_x$ for representative waveforms in the presence of

dispersion. Making use of Eq. (14) we may express $\tilde{V}_x$

$$\begin{aligned}\tilde{V}_x(\tau) &= \int_{-\infty}^{\infty}\frac{d\omega_1}{\sqrt{2\pi}}\int_{-\infty}^{\infty}\frac{d\tau'}{\sqrt{2\pi}}\tilde{V}_0(\tau')e^{-j\omega_1\tau'}\exp\left\{j\Phi(\omega_1,\tau,x)\right\}\\ &= \int_{-\infty}^{\infty}d\tau'\,\tilde{V}_0(\tau')G(\tau-\tau',x),\end{aligned} \tag{18}$$

in terms of the propagator,

$$G(\tau,x)=\frac{1}{2\pi}\int_{-\infty}^{\infty}d\omega_1\exp\left\{j\Phi(\omega_1,\tau,x)\right\}. \tag{19}$$

In the absence of dispersion, *i.e.*, when second and higher derivatives of wavenumber are negligible. $G(\tau,x)=\delta(\tau)$. In this case $\tilde{V}_x(\tau)=\tilde{V}_0(\tau)$ and we recover the familiar result, $V(t,x)\approx\tilde{V}_0\left(t-x/V_g\right)\exp\left[j\omega_0\left(t-x/V_\varphi\right)\right]$, where the constant phase-fronts travel at the phase-velocity $V_\varphi=\omega/\beta$, and modulation in $\tilde{V}_0$ travels at the group velocity $V_g=1/\beta'(\omega_0)$. Our interest is to analyze the Eqs. (18) and (19) including dispersion, and for a specific initial waveform corresponding to an incident square-wave,

$$\tilde{V}_0(t)=H(t)H\left(T_p-t\right)=\begin{cases}0\,;t<0\\1\,;0<t<T_p\\0\,;T_p<t\end{cases}, \tag{20}$$

with *H* the step-function. This corresponds in the frequency domain to

$$\tilde{V}(\omega_0+\omega_1,0)=\int_{-\infty}^{\infty}\frac{d\tau'}{\sqrt{2\pi}}\tilde{V}_0(\tau')e^{-j\omega_1\tau'}=\int_0^{T_p}\frac{d\tau'}{\sqrt{2\pi}}e^{-j\omega_1\tau'}=\frac{1}{\sqrt{2\pi}}\frac{1-e^{-j\omega_1T_p}}{j\omega_1}. \tag{21}$$

The downstream voltage phasor is just

$$\tilde{V}_x(\tau) = \int_0^{T_p} d\tau' \, G(\tau - \tau', x). \tag{22}$$

In the case that transmission is dominated by 1st-order dispersion ($\beta'' \neq 0$), and

$$G \approx \frac{1}{2\pi j} \int_{-j\infty+}^{j\infty+} dp \exp\left\{ p\tau + \frac{j}{2}\Theta'' p^2 \right\} = \frac{1}{\sqrt{2\pi j \Theta''}} \exp\left\{ \frac{j\tau^2}{2\Theta''} \right\},$$

where we introduce $\Theta(\omega, x) = \beta(\omega)x$, the cumulative phase-advance between 0 and a point *x*. Derivatives with respect to frequency, evaluated at $\omega = \omega_0$, are denoted by the prime. The downstream voltage phasor may be expressed as

$$\tilde{V}_x(\tau) = \frac{1}{\sqrt{2\,j}} \int_{-\hat{\tau}}^{\hat{T}_p - \hat{\tau}} d\hat{\tau}' \exp\left[ j \frac{\pi}{2} \sigma \, \hat{\tau}'^2 \right] = \frac{1}{\sqrt{2\,j}} \left\{ E\left(\hat{T}_p - \hat{\tau}\right) + E\left(\hat{\tau}\right) \right\}$$

where $\sigma = \operatorname{sgn}\Theta''(\omega_0)$, and the function $E$ may be expressed in terms of the Fresnel integrals

$$C(u) = \int_0^u \cos\left( \frac{\pi}{2} t^2 \right) dt, \qquad S(u) = \int_0^u \sin\left( \frac{\pi}{2} t^2 \right) dt,$$

as $E = C + j\sigma S$. We have introduced normalized coordinates,

$$\hat{\tau} = \frac{\tau}{\sqrt{\pi \left| \Theta'' \right|}}, \qquad \hat{T}_p = \frac{T_p}{\sqrt{\pi \left| \Theta'' \right|}},$$

in terms of which the time coordinate is

$$t = \frac{z}{V_g} + \left(\pi|\beta''|x\right)^{1/2}\hat{\tau},$$

and the waveform shape is a universal function of $\hat{T}_p$. Inspecting these waveforms, as depicted in Fig. 9, one finds that for $\hat{T}_p$>1.46, the peak voltage is greater than or equal to the initial amplitude. Thus with first order dispersion one arrives at a simple condition for maintenance of the transient peaking voltage on the line

$$T_p > 2.59\left(|\beta''|L_s\right)^{1/2}, \tag{23}$$

where $L_s$ is the required structure length.

This waveform, distorted by first-order dispersion, will turn out to be unsatisfactory for our application, and thus we are encouraged to consider a transmission line designed for zero first-order dispersion, $\beta''(\omega_0) = 0$. Neglecting third and high-order terms, we have

$$G \approx \left(\tfrac{2}{\Theta'''}\right)^{1/3} Ai\left(-\left(\tfrac{2}{\Theta'''}\right)^{1/3}\tau\right),$$

with *Ai* the Airy function,

$$Ai(u) = \int_0^\infty d\xi \cos\left\{\frac{1}{3}\xi^3 + u\xi\right\}.$$

In this case the natural normalization for time is

$$\hat{\tau} = \left(\frac{2}{\Theta'''}\right)^{1/3}\tau, \qquad \hat{T}_p = \left(\frac{2}{\Theta'''}\right)^{1/3} T_p, \tag{24}$$

and the downstream waveform is,

$$\tilde{V}_x(\tau) = \int_{\hat{\tau}-\hat{T}_p}^{\hat{\tau}} du\, Ai(-u).$$

Results for dispersion of square-waves of various lengths are illustrated in Fig. 10. Inspecting such plots, one finds that for $\hat{T}_p \geq 2.3$, the maximum voltage is greater than or equal to the initial voltage amplitude. In terms of unnormalized coordinates,

$$t = \frac{x}{V_g} + \left(\frac{\beta''' x}{2}\right)^{1/3} \hat{\tau}, \qquad T_p = \left(\frac{\beta''' x}{2}\right)^{1/3} \hat{T}_p, \tag{25}$$

the pulse length requirement is

$$T_p \geq 1.8\left(\beta''' x\right)^{1/3}. \tag{26}$$

Next let us make this result more definite by applying it in the case of a particular dispersion relation, for simplicity, a single-period transmission line, with dispersion relation

$$\cos\theta = \frac{\omega_0^2 - \omega^2}{\kappa\omega_0^2}. \tag{27}$$

We treat the coupling factor $\kappa$ as a constant. The cell resonance frequency is $\omega_0$, and $\theta$ is the phase advance per cell, $\theta(\omega) \equiv \beta(\omega) w_2$. The group velocity is determined from

$$\theta' = \frac{2\omega}{\kappa\omega_0^2 \sin\theta}, \tag{28}$$

according to

$$\frac{V_g}{c} = \beta_g = \frac{w_2}{c}\frac{1}{\theta'}, \tag{29}$$

with $w_2$ the cell period. In fact, having chosen $w_2 = \lambda/\sqrt{2}$, we may express

$$\beta_g = 2^{1/2}\pi\left(\frac{d\theta}{d\ln\omega}\right)^{-1}, \qquad \text{or} \qquad \theta' = \frac{2^{1/2}\pi}{\beta_g\omega}. \tag{30}$$

With one more differentiation one can show that the condition for zero first order dispersion is

$$\tan\theta = \omega\theta' = \frac{2^{1/2}\pi}{\beta_g}, \tag{31}$$

and this implies that phase-advance per cell is fixed, and, for low group velocity, near π/2, modulo π (*i.e.*, mid-band). After more algebra one obtains the second-order dispersion,

$$\theta''' = (\theta')^3\sin\theta \approx \left(\frac{2^{1/2}\pi}{\beta_g\omega}\right)^3. \tag{32}$$

With these results we may derive a lower bound on group velocity from the lower bound on pulse length. Our dispersion formulae call on the cumulative phase-shift to a point *x*,

$$\Theta''' = N\theta''' = \left(\frac{2^{1/2}\pi N^{1/3}}{\beta_g\omega}\right)^3, \tag{33}$$

and we consider the last cell in the secondary transmission line, so that $x = Nw_2 = L_s$. The normalized time coordinate is

$$\hat{\tau} = \left(\frac{2}{\Theta'''}\right)^{1/3} \tau = \frac{\beta_g \omega \tau}{2^{1/6} \pi N^{1/3}}, \tag{34}$$

and the normalized pulse length is

$$\hat{T}_p = \left(\frac{2}{\Theta'''}\right)^{1/3} T_p = \frac{\beta_g \omega T_p}{2^{1/6} \pi N^{1/3}} = 2^{5/6} \beta_g \frac{N_c}{N^{1/3}}, \tag{35}$$

with $N_c = f T_p$ the number of cycles and $f = \omega / 2\pi$ the frequency. Thus for $\hat{T}_p \geq 2.3$, corresponding to Eq. (26), we require

$$\beta_g \geq 1.3 \frac{N^{1/3}}{N_c}. \tag{36}$$

For comparison we note that where first order dispersion dominates, taking a $2\pi/3$ mode synchronous structure as an example, the corresponding constraint is $\beta_g > 0.66\, N^{1/2} / N_c$.

The foregoing assumed a lossless, constant-impedance line. To include the effects of losses and tapering, we redefine

$$\tau = t - \int_0^x dx'\, \beta'(\omega_0, x), \tag{37}$$

and express

$$\tilde{V}_x(\tau) = \int_0^{T_p} d\tau'\, G(\tau - \tau', x) e^{-\mu(x)}, \tag{38}$$

where

$$\frac{d\mu}{dx} = \frac{1}{2V_g}\left(\frac{\omega}{Q_{w2}} + \frac{dV_g}{dx}\right). \tag{39}$$

The propagator satisfies

$$\frac{\partial G}{\partial x} \approx \frac{1}{6}\beta'''(x)\frac{\partial^3 G}{\partial \tau^3}, \tag{40}$$

in the limit of negligible first-order dispersion. With a change of variables,

$$\hat{x} = \int_0^x \frac{\beta'''(x)}{\beta'''(0)}dx', \tag{41}$$

this may be reduced to the problem of second-order dispersion on a constant-impedance line.

For the case of a linear taper in group velocity (constant $V_g'$) the dispersion constraint may be expressed in terms of the initial group velocity as

$$\beta_g(0) \geq 1.3\frac{\hat{N}^{1/3}}{N_c}, \tag{42}$$

where the effective number of cell periods is obtained by using the result of Eq. (32) in the integrand of Eq. (41),

$$\hat{N} = \frac{1}{2\Gamma}\left\{\frac{1}{(1-\Gamma N)^2} - 1\right\}, \tag{43}$$

and $\Gamma = -w_2 V_g'/V_g(0)$. The combined effect of tapering and dispersion provides a voltage attenuation exponent,

$$\mu(x) = \frac{1}{2V_g'}\left(\frac{\omega}{Q_{w2}} + V_g'\right)\ln\left(\frac{V_g(x)}{V_g(0)}\right),$$

and we will consider only the linear, constant-gradient taper, $V_g' = -\omega / Q_{w2}$, for which $\mu(x) = 0$. The maximum number of normalized periods consistent with dispersion is $\hat{N}_{\max}^{1/3} \approx \beta_g(0) N_c / 1.3$, and this figure determines the maximum number of cells in the secondary,

$$N_{\max} = \frac{1}{\Gamma}\left\{1 - \frac{1}{\sqrt{1 + 2\Gamma\hat{N}_{\max}}}\right\}. \tag{44}$$

For example, consider a line with $N \approx 50$, and $N_c \approx 30$ (a 0.33 ns pulse). For a constant-impedance, lossless line, Eq. (36) requires $V_g \geq 0.17\,c$ to maintain the transient peaking voltage on the line. The first order dispersion result gives the same limit; however, the first-order dispersed waveform tends to be more broad than that provided by the Airy function. If we include wall-losses corresponding to $Q_{w2} \approx 2.7 \times 10^3$ and constant-gradient tapering, and assume the ideal period length $w_2 \approx \lambda / \sqrt{2}$, and $V_g(0) = 0.174\,c$, the maximum number of periods from Eq. (46) is $N_{\max} \approx 35$.

With the work of this section we have quantified the bounds on secondary length and group velocity deriving from dispersion and losses. This analysis also permits a rough assessment of the effect of errors on accelerating voltage. The simplest estimate considers a constant-impedance line, an error in the drive angular frequency $\delta\omega$, and a particle timed to arrive at a position $x$, at time $t = x / V_{g0}$, where $V_{g0}$ is the design group velocity. The particle witnesses a phase $\varphi = \omega t - \beta x$, and experiences a voltage gain varying as $\cos\varphi$. Thus to attain 99% of full voltage, the phase-error should be held to $|\delta\varphi| < 0.14$. Phase-error may be related to frequency error according to

$$\delta\varphi = \delta\omega \frac{x}{V_{g0}} - \left( \beta' \delta\omega + \frac{1}{2}\beta'' \delta\omega^2 + \frac{1}{6}\beta''' \delta\omega^3 + \mathsf{K} \right) x \approx -\frac{2^{1/2}\pi^3}{3}\left( \frac{\delta\omega}{\omega}\frac{1}{\beta_g} \right)^3 N_2,$$

where in the last equality we evaluate the result at the end of the line, $x = N_2 w_2$. For the longest line consistent with dispersion, corresponding to equality in Eq. (36), this gives $\delta\omega/\omega < 0.3/N_c$ for 99% of full voltage. With $N_c \approx 30$, one requires $\delta\omega/\omega < 9\times10^{-3}$, corresponding to a 0.8 GHz tolerance for the secondary line, for our parameters. This simple estimate is however too generous as the practical concern is not a drive-frequency error, but errors in cell-tuning. In the case of random errors with root-mean-square (rms) $\sigma_\omega$ one has

$$\delta\varphi \approx \frac{\sigma_\omega}{\omega}\frac{\sqrt{N_2}}{\beta_g}.$$

In this case, 99% of full-voltage at the last cell requires $\sigma_\omega/\omega < 0.2/N_c N_2^{1/6}$. Or $\sigma_\omega/\omega < 3\times10^{-3}$ (0.27 GHz) for $N_c \approx 30$ and $N_2 \approx 50$. In the case of a uniform error in tune, as for a scale error, one has $\delta\omega/\omega < 0.2/N_c N_2^{2/3}$, or $\delta\omega/\omega < 5\times10^{-4}$ (0.05 GHz). To translate such tolerances on cell-tune into dimensional tolerances, a detailed electromagnetic design is required, and this is provided in Sec. IV.

### *D. Coupled-Cavity Simulation*

To check the foregoing analysis we consider a more detailed model for the secondary line as a chain of *n=1,2,...N* coupled cavities,[18] as illustrated in Fig. 11. Each cell is characterized by cell voltage $V_n$, evolving as a simple-harmonic oscillator perturbed by wall losses, coupling to the nearest neighbor cells, and external coupling (for the end cells),

$$\left( \frac{\partial^2}{\partial t^2} + \frac{\omega_n}{Q_n}\frac{\partial}{\partial t} + \omega_n^2 \right) V_n = \frac{1}{2}\omega_n^2 \left( \kappa_{n-1/2} V_{n-1} + \kappa_{n+1/2} V_{n+1} \right) + 2\frac{\omega_1}{Q_{e1}}\frac{\partial V_F}{\partial t}\delta_{n,1} - 2k_l \frac{\partial I_n}{\partial t}. \qquad (45)$$

The forward-going voltage in the connecting guide has been transformed to $V_F$, and reverse waveform $V_R$, satisfying continuity of tangential electric field,

$$V_1 = V_F + V_R. \tag{46}$$

The absence of external drive for the last cell corresponds to the assumption of a matched load at the output. The beam current $I_n$ is specified by the bunch schedule. The Kronecker delta function $\delta_{n,1} = 1$ for $n$=1, and otherwise is zero. The $Q$ of each cell is determined by the wall $Q$, and, for the end-cells, $n$=1, $N$, external coupling,

$$\frac{1}{Q_n} = \frac{1}{Q_{en}} + \frac{1}{Q_{wn}}, \tag{47}$$

The geometry of the coupling hole between cells determines the coupling constants $\kappa_{n-1/2}$. The cell resonance frequencies $\omega_n$ are determined by the cell geometry with perturbations due to the coupling slots and the beam-tube. For a strictly periodic structure, the coupling coefficients and cell resonance frequencies are constant over the interior cells.

To determine the desired values for circuit parameters we analyze this system in the frequency domain, with no beam-drive. We consider a steady-state excitation, at the center-band design angular frequency $\omega$, so that $V_n = \Re \tilde{V}_n e^{j\omega t}$. In terms of the propagation constant $\gamma = j\theta + \Gamma$, we may relate adjacent cell voltages according to $\tilde{V}_n \approx \tilde{V}_{n\pm1} e^{\pm\gamma}$, and this permits us to solve for the interior cell resonance frequencies in terms of the phase-shift per cell,

$$\omega_n = \frac{\omega}{\sqrt{1 - \kappa_n \cos\theta}}. \tag{48}$$

The coupling constants are determined from the design local group velocity

$$\kappa_n = \frac{\beta_{gn}}{\frac{1}{2}\varphi\sin\theta + \beta_{gn}\cos\theta}, \tag{49}$$

with $\varphi = \omega L / c$. One can show that to maintain negligible first order dispersion the phase-advance per cell should satisfy $\tan\theta = \varphi / \beta_g$, and this is near $\pi/2$ modulo $\pi$. The attenuation parameter per cell is determined for a constant-impedance line to be $\Gamma \approx \omega / \kappa_n \omega_n Q_{wn} \sin\theta$, and for a constant-gradient line, $\Gamma \approx 0$; these are the two cases we will be considering. Matching conditions are obtained from the frequency-domain analog of Eq. (45) for the end-cells, and employing the line propagation characteristic. So, for the input cell,

$$\left( j\frac{\omega\omega_1}{Q_1} + \omega_1^2 - \omega^2 \right)\tilde{V}_1 = \frac{1}{2}\omega_1^2 \kappa_i \tilde{V}_2 + 2j\frac{\omega\omega_1}{Q_{e1}}\tilde{V}_F. \tag{50}$$

The condition for a match at angular frequency $\omega$ corresponds to $\tilde{V}_R = \tilde{V}_1 - \tilde{V}_F = 0$. Substituting $\tilde{V}_2 \approx \tilde{V}_1 e^{-\gamma}$ in Eq. (50) one obtains

$$\omega_1 \approx \frac{\omega}{\sqrt{1 - \frac{1}{2}\kappa_i\left(1-\Gamma\right)\cos\theta}}, \tag{51}$$

$$\frac{1}{Q_{e1}} \approx \frac{1}{Q_w} + \frac{1}{2}\frac{\kappa_i\left(1-\Gamma\right)\sin\theta}{\sqrt{1 - \frac{1}{2}\kappa_i\left(1-\Gamma\right)\cos\theta}}, \tag{52}$$

The output coupler cell satisfies

$$\left( j\frac{\omega\omega_N}{Q_N} + \omega_N^2 - \omega^2 \right)\tilde{V}_N = \frac{1}{2}\omega_N^2 \kappa_o \tilde{V}_{N-1}, \tag{53}$$

and substituting $\tilde{V}_{N-1} \approx \tilde{V}_N e^{\gamma}$, one obtains

$$\omega_N \approx \frac{\omega}{\sqrt{1-\frac{1}{2}\kappa_o(1+\Gamma)\cos\theta}}, \tag{54}$$

$$\frac{1}{Q_{eN}} \approx -\frac{1}{Q_w} + \frac{1}{2}\frac{\kappa_o\left(1+\Gamma\right)\sin\theta}{\sqrt{1-\frac{1}{2}\kappa_o(1+\Gamma)\cos\theta}}. \tag{55}$$

These results determine the end-cell detunings and the external $Q$ parameters for a match at center-band, as a function of the input and output cell coupling parameters $\kappa_i$ and $\kappa_o$. These are free parameters affecting the bandwidth of the match, with two distinguished choices. If the first coupling slot geometry is desired to match the other cells in dimension, it may be determined from the group velocity profile, so that $\kappa_i = \kappa_{3/2}$. Alternatively, we may ask that the coupler cavity be driven as though it were part of an infinite structure. In this case, the natural resonance frequency of the first cavity should be the same as those nearby, so that $\kappa_i = 2\kappa_{3/2}$. This choice gives the best match for a transient pulse.

With the circuit parameters determined, the system may be solved numerically, in the time-domain, by means of a leap-frog algorithm. Alternatively, one may express cell voltages as $V_n = \Re\tilde{V}_n(t)e^{j\omega t}$, and solve Eq. (45) in the slowly-varying envelope approximation, $\left|d\tilde{V}_n/dt\right| << \omega\left|\tilde{V}_n\right|$. This involves a leap-frog time-advance, and a tri-diagonal matrix inversion at each time-step; this approach is more computationally efficient as it permits a larger time-step.[8] For studies of beam-loading, note that single point-bunch excitation by a charge $q_b$ amounts simply to a displacement of the cavity phasor referred to beam-phase, $\tilde{V}_n \to \tilde{V}_n - 2k_l q_b$, at the time of bunch passage. For numerical studies, we will adopt the simplest of bunch schedules, timing the bunches to arrive at the maximum in cell voltage, and phased for maximum acceleration.

With the scalings of this section, and the coupled-cavity model, we are equipped to study a numerical example to illustrate the design and performance of such a matrix accelerator.

## III. EXAMPLE DESIGN

In this section we employ the scalings derived in Sec. II to arrive at an example design. One caveat should be added at this point, that we have not provided a rigorous analytic formulation of the effect of beam-loading on the transient waveform. The most conservative estimate would *add* beam-induced voltages, such that the voltage in the last cell is loaded by an amount $2k_l N_2 q_b$. In fact, however, a bunch passing through the device modifies the shape of the net waveform downstream. To provide a rigorous accounting for beam-loading on the transient waveform, we will consult the coupled-cavity model.

To illustrate the scalings we provide in Table 1, three example parameter sets. In column (a), charge is low and beam-loading is neglected. In column (b) beam-loading is accounted for with the conservative estimate, requiring a 16% over-voltage in the first cell. In column (c) we consider a low group velocity, and a correspondingly smaller number of beamlines. Other parameters are $N_1 = 25$, $Q_{w2} \approx 2.7\times10^3$, $Q_{w1} \approx 9.94\times10^3$, $[R/Q] = 221\,\Omega$, $2Q_{w2}/\omega$=9.4 ns, $T_p \approx 0.33$ ns. Pulsed temperature rise is the same for the primary and the secondary. Minimum gradient is 1.01 GeV/m at the last cell. To illustrate the design considerations, we discuss column (b) in detail, and then discuss simulation results.

We start from an assumed requirement on gradient at the output end of the device, after beam-loading, of $G \approx 1.01$ GeV/m, and a total charge requirement of $N_2 q_b \approx 3$ nC, where the charge per secondary beamline, $q_b$, and the number of secondary beamlines, $N_2$, have yet to be determined. The critical inputs at this point correspond to a specification of the geometry. We assume the ideal dimensions $a = w = \lambda/\sqrt{2} \approx 0.232$ cm, and transit angle of $133.6°$ for optimum $[R/Q] \approx 221\,\Omega$ and $Q_{w2} \approx 2.7\times10^3$. Gap length is then $L \approx 0.122$ cm. The minimum cell voltage is then $V_c \approx GL \approx 1.23\times10^6$ V. Loss-factor is determined from $[R/Q]$ to be $k_l \approx 32$ V/pC. Our conservative estimate of net beam induced voltage is then $2k_l N_2 q_b \approx 1.95\times10^5$ V or 15.7% of the net voltage in the last cell. According to this estimate, the line must be operated at an overvoltage corresponding to a gradient in the first cell of 1.17 GeV/m. In the first cell of the secondary line peak cavity

voltage is $V_{NL} \approx 1.42 \times 10^6$ V, and the corresponding energy per cell is $U_2 = V_{NL}^2 / 4k_l \approx 15.9$ mJ.

The maximum ("hot-spot") power dissipation on the secondary walls is then fixed at $3.06 \times 10^{11}$ W/m$^2$, and the pulsed temperature rise is determined by the choice of $T_p$. For the choice of primary mode number $m \approx 15$, the discharged pulse length is $T_p \approx 0.33$ ns, and $\Delta T \approx 168$ K. For a 120 Hz machine repetition rate, the duty cycle is $4 \times 10^{-8}$, and thus time-averaged power dissipation is 1.2 W/cm$^2$ at a hot-spot.

At this point we must choose a figure for the initial group velocity in the secondary line, realizing that too low a value will limit the number of cells, $N_2$, on account of dispersion and attenuation. We select $V_{g2}(0) = 0.174c$, for which the maximum number of cells with a constant-gradient, linear taper is $N_2 \approx 35$. This taper brings the group velocity to $0.116c$ at the output.

The peak power required from the discharging primary cell is then determined by the product of the group velocity and the local energy density in the secondary $U_2 / w_2 \approx 6.9$ J/m, and is $U_1 / T_p \approx 3.58 \times 10^8$ W. The stored energy requirement in one primary cell is $U_1 \approx 0.12$ J. The energy density in the primary line prior to discharge is then $U_1 / L \approx 96$ J/m. This figure for energy density is critical to the energetics and efficiency of a linac premised on the matrix design. For our parameters, we will be providing $3$ nC $\times 1$ GeV/m $\approx 3$ J/m to the beam. This corresponds to a 3.1% efficiency of transfer of energy from the primary to the beam. The implication is then that for a collider, with a total of two 3 nC beams accelerated to 2.5 TeV, running at 120 Hz, the average beam power would be 1.8 MW, and the site power load due to the mm-wave system would be $57$ MW$/\eta_{\rm rf}$. The factor $\eta_{\rm rf}$ is the product of all efficiencies from wall-plug to stored energy in the primary, a significant factor amounting to between one and two orders of magnitude.[19] For a critically coupled primary cavity, operated with $\tau_1 \approx 1.05$, the pulsed temperature rise is the same as that of the secondary, and the power required by the primary is $P_1 \approx 4.0 \times 10^2$ MW in a 18.2 ns pulse. With these choices, the efficiency of transfer of energy from the primary input to the secondary cells is 40%. Thus if one wished to hold

the machine power requirement to 500 MW, one would require a very high efficiency from wall-plug to the primary input of 30%.

To check these scalings, and to rigorously quantify the combined effect of dispersion, wall-loss, tapering and beam-loading, we employ the coupled cavity formulation. We adopt $\kappa_o \approx 2\kappa_{N-1/2}$ to provide the most broad-band match at the output and input. For the simulations we will employ $N_2 = 50$; this permits inspection of the result for $N_2 = 35$, while providing also a view of the voltage droop due to dispersion beyond this length. We employ 21.4% loading distributed over 50 beamlines as this interpolates to the requisite 15% loading at the 35th beamline.

To clarify the input coupling from the primary line, we show in Fig. 12 the forward and reverse voltages, and the cell voltage in the input cavity. In Fig. 13, representative waveforms along a constant-gradient line are illustrated. To appreciate the effects of losses, tapering and beam-loading, results for maximum cell voltages are illustrated in Fig. 14, for various conditions. For the lossless case, Eq. (36) predicts that the peak voltage will droop to unity in 50 periods, and this agrees with the result shown in Fig. 14. For the lossy constant- impedance example seen in Fig. 14, the output voltage is reduced to 0.8 after 50 periods, consistent with the 2 dB insertion loss one would expect from the steady-state scalings. For the case of attenuation in a constant-gradient structure, the result of Eq. (44) ($N_2 = 35$) is consistent with the results seen in Figs. 13 and 14, *i.e.*, the transient peaking voltage is maintained at or above unity out to the 35th beamline. The simulation also reveals that the cumulative effect of beam-loading on the transient peaking voltage is about 1/3 of that obtained from the conservative, steady-state estimate. For this case, 95% of full-voltage (unity) is attained at cell #35, where the simplest estimate would have given 85% of full-voltage. Thus the parameters of Table 1, column (b), reflect an *overestimate* of beam-loading, corresponding to a gradient varying from 1.4 GeV/m to 1.1 GeV/m in the last cell. The actual figures for a last-cell gradient of 1.01 GeV/m and 3 nC are closer to column (a).

The foregoing discussion illustrates the scalings for a particular example. While we have premised the example on maintenance of the transient peaking voltage on the line, we note that the collider application[16] actually favors a droop of about 15% across the beamlines. The example illustrated in Fig. 13 shows that this corresponds to 50 periods. With 3 nC divided over 50 beamlines the charge per bunch is 60 pC, and this is a more

tolerable figure for the transverse dynamics of the beam in a realistic collider lattice. It is worth remarking that for the constant-gradient, loaded curve illustrated in Fig. 14, the peaking cell voltage corresponds, after an overshoot of 30% in the first cell, to a a linear variation from 1.2 to 1.06 over the first 25 cells. Thus where fewer beamlines are required the scalings are more favorable than the Table 1 parameters would indicate, *i.e.*, in the early beamlines the gradient is augmented by 20% due to the character of the transient discharge.

## IV. CAVITY DESIGN

In this section we provide an electromagnetic design for the accelerating cells of the secondary line, and a design for a 7-cell prototype matched to standard WR10 waveguide. For computations we employ the finite-difference code GdfidL.[20] We don't achieve the ideal [*R/Q*] with this geometry; however, we feel detailed optimization of the geometry is best left to a later work. In the meantime, the geometry we consider has the virtue of simplicity.

### *A. Single-Cell*

We analyze a pillbox design very much like that of Fig. 8 consisting of rectangular guide, with cylindrical beam tubes and rectangular coupling slots, as illustrated in Figs. 15 and 16, with dimensions listed in Table 2. We emphasize that these are rough dimensions in that the geometry is still somewhat idealized, not incorporating the effects of filleting or corner rounding, nor special-features to enhance [*R/Q*].

The dimensions shown in Fig. 15 were arrived at starting from the optimized closed pillbox and adjusting slit dimensions (width $t$ and gap $2d$), to arrive at a reasonable $[R/Q]$ and the desired group velocity. Frequency domain calculation with the geometry of Fig. 16, and magnetic boundary conditions at the plane $x$=0, and electric boundary conditions at the mid-plane of the adjacent cell ($x$=$L$) gives $[R/Q] \approx 144\,\Omega$, and $Q_w \approx 2.3\times 10^3$, and a resonance frequency of 91.392 GHz. The corresponding phase-advance per cell is $3\pi/2$. A lower-frequency $\pi/2$ mode occurs at 63.7 GHz, with $[R/Q] \approx 39\,\Omega$ and $Q_w \approx 7.7\times 10^2$. Employing magnetic boundary conditions at both planes, the frequency-domain calculation provides the frequencies for $\pi$ and 0 modes: 87.0 GHz and 95.5 GHz. These results can be

employed to infer the group velocity at the design frequency, by fitting to the simple two-parameter periodic line dispersion relation $\omega^2(\theta) = \omega_0^2(1 - \kappa\cos\theta)$. This gives $\kappa \approx -0.093$, and

$$\beta_g = \left(\frac{\omega_0 w_2}{c}\right)\left(\frac{\omega_0}{\omega}\right)\frac{\kappa}{2} \approx -0.24. \tag{56}$$

To gauge the dimensional tolerances required, we have surveyed errors in each of the major dimensions, with the results listed in Table 3. In addition, to assess sensitivity to bonding, a 164 $\mu$m (6.5 mil) gap was inserted between the coupling irises and the roof and floor, as illustrated in Fig. 17(a). This shifted the mode frequency by -2.1% (-1.89 GHz), and raised the $[R/Q]$ by 14% to $165\Omega$, and the wall $Q$ by 16% to $2.7\times10^3$. When the gap was reduced to 33 $\mu$m (1.3 mil), the frequency shift was -1.7% (-1.6 GHz), $[R/Q] \approx 162\,\Omega$, and $Q_w \approx 2.0\times10^3$. We conclude that bonding would be critical for proper tune, in this design. However, the salubrious effect of the gap on $[R/Q]$ suggests that future work attend to a design *incorporating* such a gap, if mechanical stability of cantilevered coupling irises should prove workable. To assess the effect of filleting, a $127\mu\text{m}\times127\mu\text{m}$ ($5\,\text{mil}\times5\,\text{mil}$) vertical post was placed in the corner of one cell, as illustrated in Fig. 17(b). This raised the mode frequency by 0.5% (+0.48 GHz), had negligible effect on $[R/Q]$, and raised the wall $Q$ by 0.1%. A smaller, $2\,\text{mil}\times2\,\text{mil}$ post produced a frequency shift of +0.08 GHz or 0.1%. Filleting and bonding must be accounted for in a final design.

To translate these results into geometrical tolerances one must consult the accelerator requirements, as discussed in Sec. II.C. For example, we found that for 99% of no-load voltage with $N_c \approx 30$ and $N_2 \approx 50$, rms cell-tuning error should be less than 0.27 GHz. The corresponding dimensional tolerances are listed in the right-most column of Table 3, and the smallest of these is 1/2 mi1 (0.0005"). Tolerances on scale errors are smaller by a factor of 6. For mechanical design, tolerances will need to be reduced further due to the presence of mutliple dimensional errors in each cell. This reduction depends on the method of fabrication, and could amount to a factor of 2.

### *B. Seven-Cell Prototype*

To illustrate the single-cell design in terms of a circuit amenable to bench measurements, we arrived at parameters for a 7-cell block as shown in Fig. 18. Numerical matching to WR10 was performed with the aid of the time-domain module of the GdfidL code, and involved shimming the outermost iris (width $t_c$ and gap $2d_c$), and adjusting the *x*-dimension, $w_{2c}$, of the outermost cavities to achieve correct coupler-cell detuning. Results from GdfidL for the S-Matrix of the seven-cell block are shown in Fig. 19. Results from the coupled-cavity model are shown in Fig. 20 for comparison, computed in the frequency domain with a tri-diagonal matrix inversion. The match is not ideal; however finer adjustment is best pursued when rounded features have been incorporated in the numerical geometry. In the meantime this example illustrates the simplest implementation of the concept, and the correspondence with the circuit model.

## V. SWITCH

The switch referred to in Figs. 5, 6, and 7 is a critical element of this design. We consider here the use of a WR10 H-plane tee, as illustrated in Fig. 21, with a layer of dielectric photoconductor embedded in port 3.

### *A. Three-Port Network as a Control Element*

To analyze this element, we first consider the tee alone. For any lossless and reciprocal three-port network, the scattering matrix is unitary and symmetric. Imposing these conditions, accounting for symmetry between the WR10 ports (ports 1 and 2) and making a choice of reference plane, the *S*-matrix may be expressed in terms of two parameters $\theta$ and $\phi$,

$$\mathbf{S}_{tee} = \begin{pmatrix} \dfrac{e^{j\phi} - \cos\theta}{2} & \dfrac{-e^{j\phi} - \cos\theta}{2} & \dfrac{\sin\theta}{\sqrt{2}} \\ \dfrac{-e^{j\phi} - \cos\theta}{2} & \dfrac{e^{j\phi} - \cos\theta}{2} & \dfrac{\sin\theta}{\sqrt{2}} \\ \dfrac{\sin\theta}{\sqrt{2}} & \dfrac{\sin\theta}{\sqrt{2}} & \cos\theta \end{pmatrix}. \tag{57}$$

The scattered signals $\underline{V}^-$ are determined from the incident signals $\underline{V}^+$, according to

$$\underline{V}^- = \begin{pmatrix} V_1^- \\ V_2^- \\ V_3^- \end{pmatrix} = \mathbf{S}_{tee}\underline{V}^+ = \mathbf{S}_{tee}\begin{pmatrix} V_1^+ \\ V_2^+ \\ V_3^+ \end{pmatrix}. \tag{58}$$

Terminating port 3 in a conducting plane corresponds to the condition $V_3^+ = V_3^- e^{j\psi}$, for some phase $\psi$. The resulting two-port network is then described by the *S*-matrix,

$$\mathbf{S} = \begin{pmatrix} \cos\left(\frac{\zeta-\phi}{2}\right)e^{j\left(\frac{\phi}{2}+\frac{\zeta}{2}+\alpha\right)} & j\sin\left(\frac{\zeta-\phi}{2}\right)e^{j\left(\frac{\phi}{2}+\frac{\zeta}{2}+\alpha\right)} \\ j\sin\left(\frac{\zeta-\phi}{2}\right)e^{j\left(\frac{\phi}{2}+\frac{\zeta}{2}+\alpha\right)} & \cos\left(\frac{\zeta-\phi}{2}\right)e^{j\left(\frac{\phi}{2}+\frac{\zeta}{2}+\alpha\right)} \end{pmatrix}, \tag{59}$$

where the angle $\zeta$ is given by

$$e^{j\zeta} = \frac{\cos\theta - e^{j\psi}}{e^{j\psi}\cos\theta - 1}, \tag{60}$$

and $\alpha$ is an angle determined by the choice of reference planes. When the switch is *off*, *i.e.*, when $S_{12} = 0$, the angle $\zeta = 2n\pi + \phi$, for some integer *n*, and $\cos\zeta = \cos\phi$. When the switch is *on*, $\cos\zeta = -\cos\phi$. The signal level in the third arm is given by

$$\begin{aligned} \left|V_3^+\right|^2 = \left|V_3^-\right|^2 &= \frac{\sin^2\theta}{3 - 4\cos\theta\cos\psi + \cos 2\theta}\left|V_1^+ + V_2^+\right|^2 \\ &= \frac{1+\cos^2\theta + 2\cos\theta\cos\zeta}{2\sin^2\theta}\left|V_1^+ + V_2^+\right|^2 \end{aligned}, \tag{61}$$

and in the last line we have solved for $\psi$ in terms of $\zeta$, from Eq. (60). Assuming that the

switch is looking at a matched load, so that $V_2^+ = 0$, one may express the signal level in the third arm in terms of the incident voltage. Thus one can determine the peak electric field $E_{\max}$ at the surface of the diamond dielectric in the off-state, neglecting evanescent mode contributions,

$$E_{\max}^2 = 4\left(\frac{1+\cos^2\theta+2\cos\theta\cos\phi}{2\sin^2\theta}\right)\left(\sin\frac{\Delta\psi}{2}\right)^2\frac{P_{in}Z_3}{A_3G_3}, \tag{62}$$

where $P_{in}$ is the constant level input power, $Z_3$ is the wave impedance of the mode excited in the waveguide that forms the third arm, $A_3$ is the cross-sectional area of that guide, and $G_3$ is a geometrical factor that depends on the mode and the waveguide shape of the third arm. For $TE_{10}$ mode of rectangular guide, $G_3 = 1/4$. Finally, the phase-shift $\Delta\psi$ corresponding to switch activation may be determined from

$$e^{j\Delta\psi} = \frac{\left(e^{j(\phi+\pi)}+\cos\theta\right)\left(1+e^{j\phi}\cos\theta\right)}{\left(e^{j\phi}+\cos\theta\right)\left(1+e^{j(\phi+\pi)}\cos\theta\right)}. \tag{63}$$

With some algebra, we find

$$E_{\max}^2 = 4\left(\frac{\sin^2\theta}{3+\cos 2\theta-2\cos(\theta-\phi)-2\cos(\theta+\phi)}\right)\frac{P_{in}Z_3}{A_3G_3}. \tag{64}$$

In the on-state, losses in the dielectric are determined from

$$P_l = \left(\frac{1+\cos^2\theta-2\cos\theta\cos\phi}{2\sin^2\theta}\right)\frac{R_s}{Z_3}P_{in}, \tag{65}$$

where

$$R_s = \left( \frac{\omega \mu_0}{2\sigma} \right)^{1/2} \tag{66}$$

is the surface resistance of the active element, and $\sigma$ depends on the level of excitation.

### *B. Considerations for the Photoconductor*

As to the choice of photoconductor for the switch, we are interested in diamond due to a number of its unusual properties. Diamond has a high thermal conductivity $\kappa \approx 1.5 - 2.0 \times 10^3$ W/K – m,[21] and experience with diamond as a photoconductor indicates that unipolar fields of order 1 GV/m can be held off on a μs time scale.[22] In addition, the loss tangent is quite low, $\tan\delta < 5 \times 10^{-4}$ at W-Band.[23] Not all features of diamond are convenient for this application, however. Temperature coefficient of expansion is $\alpha \approx 1.2 \times 10^{-6}$ /°C, and thus differential expansion relative to the substrate is an issue. Field emission and secondary electron emission are practical concerns. As to the circuit performance, the effective mobility of electrons and holes in diamond drops quickly for carrier densities greater than $n_e \approx 10^{16}$ cm$^{-3}$.[24] Increasing the excitation level in diamond to exceed this value does not help to increase the conductivity by any appreciable amount. At $n_e \approx 10^{16}$ cm$^{-3}$ the conductivity in diamond is about $6.4 \times 10^2$ mho/m. This relatively low value can be compensated for to some degree by the proper choice of $Z_3$, and the angles $\theta$ and $\phi$. The skin depth of the 91.392 GHz signal with $n_e \approx 10^{16}$ cm$^{-3}$ is approximately $\delta \approx 66\ \mu$m. Hence the choice of laser wavelength required to excite the electron-hole plasma layer should have an absorption depth less than this value, and the diamond slab should have a thickness of this order. In contrast to previous work using 3rd-harmonic Nd:YAG for excitation,[25] good absorption here favors direct ionization by ultraviolet photons. The bandgap is $\varepsilon \approx 5.5$eV, so that excitation by 220 nm wavelengths or shorter is required. The *absorbed* fluence is then $F \approx n_e \delta \varepsilon \approx 60 \mu$J/cm$^2$. The absorption coefficient for uv photons is well in excess of $10^2$ cm$^{-1}$ so that the required laser fluence is less than 0.1 mJ/cm$^2$. Carrier lifetime depends on the purity, and can range from 15 ns down to the

30 ps range, with a value of 1 ns noted in [24] for synthetic diamond; this is well above the 0.33 ns mm-wave pulse length, and thus adequate for our purposes.

The design for the switch geometry consists of an H-plane tee in WR10, with a diamond layer placed in port #3, the vertical stub. The stub width is $W = 0.12"$ (0.305 cm) in *x*, the signal propagation direction, and along the electric field orientation the width is $b = 0.05"$ (0.127 cm) as for WR10. Thus the cross-section of the diamond layer is $3.9\times10^{-2}\ \mathrm{cm}^2$, and for a depth of $66\ \mu\mathrm{m}$, the volume of diamond is $V = 2.6\times10^{-4}\ \mathrm{cm}^{-3}$. At a laser fluence of $0.1\ \mathrm{mJ/cm}^2$, the required laser pulse energy to activate one switch is less than $5\ \mu\mathrm{J}$.

The parameters of the scattering matrix for the hollow tee are calculated with HFSS, using reference planes corresponding, in Fig. 21, to $L_1 \approx 0.1492"$ and $D \approx 0.0835"$. The numerical data are fit according to our analytic model to produce the two independent parameters, $\theta \approx 0.861\ \mathrm{rad}$, and $\phi \approx -0.560\ \mathrm{rad}$. These parameters and the dielectric constant for diamond $\varepsilon/\varepsilon_0 \approx 5.65$, constrain the placement of the diamond in the stub. In terms of $\theta$ and $\phi$ the result for the losses during the on state comes to 1.5% or 1.5 mJ for each $0.1$ J discharged. The volume specific heat capacity of diamond is $C \approx 1.81\ \mathrm{J/cm}^3\,\mathrm{K}$, corresponding to a heat capacity of $4.7\times10^{-4}\ \mathrm{J/K}$ for the volume *V*. Thus the pulsed temperature rise in the diamond due to mm-wave losses is about 3 K for each $0.1$ J of mm-wave energy discharged from a primary cell. The peak electric field may be expressed in terms of input power as $E_{\max}(\mathrm{GV/m}) \approx 1.29\sqrt{P_{in}(\mathrm{GW})}$. This is below the breakdown threshold of diamond for power levels considered in the examples, and is lower than the field in the accelerating cavities.

## VI. DISCUSSION

A number of issues are raised by this concept and not addressed in this analysis. Intrinsic issues are: transverse particle deflections due to the asymmetry of the signal and beam axes, higher multipole content in the fields, cross-talk between secondary lines and performance as a two-dimensional circuit.

As to transverse particle deflections, a simple estimate of the transverse kick in the geometry of Fig. 3, with periodic loading added, may be obtained by considering the electromagnetic fields as a superposition of $TE_{10}$ mode forward and reverse waves in the unloaded guide. When the signal and beam propagation axes are orthogonal one can show that the transverse kick is just the longitudinal kick multiplied by $\beta_g = V_g / c$, where $V_g$ is the group velocity on the loaded line, and $c$ is the speed of light. According to this estimate, the kick may be compensated by permitting an angle $\theta \approx \beta_g$ deviation from orthogonality. However, this estimate fails to account for the field behavior in the vicinity of the beam ports, and a more rigorous treatment remains to be performed to demonstrate a geometry and a mode of operation where the transverse voltage gradient has been zeroed on the beam-axis --- a necessary and sufficient condition for the absence of deflection, according to the Panofksy-Wenzel theorem.[26]

More generally, one can show that voltage witnessed by the beam is a harmonic function of the transverse coordinates, and therefore may be expressed as a sum of multipoles. Thus one is concerned not merely with the monopole (accelerating) and dipole (deflecting) components, but quadrupole (focusing) and higher components as well. To expand on this, in a conventional, cylindrical structure, symmetry forbids the mixing of multipoles, and excitation of the accelerating mode is not accompanied by transverse deflections. In planar structures, as considered by Henke,[27] for a conventional accelerator circuit, where inversion symmetries in *x* and *y* are respected, the lowest order multipole is quadrupolar. In this case, acceleration is accompanied by focusing or defocusing, phase-dependent kicks. In the concept presented here, inversion symmetry in *x*, while respected by the geometry, is lost due to the character of the solution (a travelling-wave in *x*). In this work, we have characterized the monopole features only, and significant work remains to design either an angled geometry with no intrinsic kick, or an external kick-compensation technique.

In addition, cross-talk between secondary beamlines has been neglected in this work. Where a conventional accelerator circuit bears comparison to a one-dimensional crystal, the circuit considered here has, in the presence of cross-talk, a two-dimensional character. In light of other work on accelerator geometries with this character,[28] we are reluctant to conclude that cross-talk is a "bug" in the design, as it could turn out to be a

useful feature.

Other interesting issues include miniature magnetic lattice design, and wakefields. One is interested to know what geometrical features of the secondary cell will promote $[R/Q]$ for the accelerating mode, while permitting a wider beam-tube, and therefore lower wakefields. For reference we note that our electromagnetic modelling puts the lowest dipole modes in D-Band, near 140 GHz. Closely tied to his question is the matter of optimal $[R/Q]$. The cell design presented here will benefit from additional refinement, including cavity-shaping, alternative cavity coupling elements, corner-rounding, and filleting. The results for $[R/Q]/L \approx 112$ kΩ/m and $Q_w \approx 2.3\times10^3$ are low compared to the ideal values, 183 kΩ/mand $2.7\times10^3$, and further work is required here. One obtains some glimpse of potential improvements in Fig. 17 (a), where an air-gap resulted in $[R/Q]/L \approx 128$ kΩ/m and a wall $Q$ equal to the ideal value. For simplicity in this work, we have restricted ourselves to the most straightforward cell geometry, and additional design studies are called for.

In addition to the theoretical issues, numerous practical concerns are raised by this concept. Prospective cell geometries must be manufacturable. Realistic surface finish and good bonding of current-carrying joints are critical to attaining good $Q$ values and correct cavity tune.[29] Structure fabrication for the high $Q$ primary geometry, may require machining tolerances in the $5\mu$m range, at the state-of-the-art in electrodischarge machining.[30] We point out however, that having separated to some degree the functions of resonant energy storage and acceleration, in the form of a primary and a secondary structure, one is freed to contemplate in-situ tuning of the primary line, without risk to the accelerating field-line shape, and without the complexity of mult-cell tuning. Where achievable tolerances and available test and measurement equipment permit, one would be interested to push the concept to still shorter wavelengths. In the THz frequency range, with its smaller depth dimensions, semi-conductor fabrication techniques may be applicable.

For high-power operation, experimental studies of field-emission, breakdown, and pulsed-heating problems will ultimately determine the gradient achievable with this concept. For such studies, a high-power amplifier at W-Band is required, and a planar free-electron laser appears promising for this application.[31] Such a tube may require in addition a pulse

compression system. *Passive* pulse compression[32] will not be suitable to match the $10^{-6}$-s modulator time-scale to the $10^{-8}$-s primary-line fill time-scale; thus *active* pulse compression is necessary.[33] An alternative to the tube as a driver is the *two-beam accelerator* concept.[14] Such a research direction benefits from previous demonstrations of peak power in the gigawatt range,[34] well in excess of that required here.

Field-emission and breakdown are concerns that we have not addressed in this work. Insofar as these phenomena presently limit accelerators, understanding is largely phenomenological, and in the range of wavelength and time-scale considered here, data are not available. Experimental studies of such transient and parasitic phenomena are fundamental to a working test accelerator, whether it be copper, dielectric or plasma. The more fundamental problem for a *conducting* structure is the matter of pulsed heating. The numerical examples we chose for illustration corresponded to a large figure for the pulsed temperature rise. The fundamental question is: what cyclic temperature rise *is* achievable in a solid-state structure? An important aspect of this problem is that fatigue-induced failure does not in itself harm the accelerating circuit, unless it disrupts wall-current, causing detuning and $Q$-degradation. In the meantime, we have shown that the temperature-derived gradient limits for conventional passive copper structures are not optimal, and one can do better.

To conclude, in this work we have introduced and analyzed a new concept for an accelerator, without too much geometrical embellishment. Additional refinements are worth pursuing. Design with a $90°$ transit angle ($Q_w \approx 2.2\times10^3$) could reduce the stored energy requirement by a factor of 1.3; the actual $[R/Q]/L$ achievable, however, depends on the minimum acceptable width of the walls separating the secondary lines, a matter of mechnical integrity in the fabrication process. Our treatment here actually opens up new possibilities for fabrication techniques, in that the secondary-line geometrical tolerances found here are more generous than one would expect from scaling of conventional structures to W-Band. In view of this, it would be interesting to relax the single-depth constraint we have accepted. This could permit a larger volume primary cavity geometry and a higher wall $Q$. In this limit, pulsed heating in the primary would be reduced, as would peak power and energy-density requirements. In light of the analysis presented, we

believe the ideal configuration would have a longer primary cavity, with $Q$ and vertical dimension larger by a factor of $O(10^1)$. In this limit one could power a 1-m, 1-GeV, $N_2 \approx 15$ beamline linac with a single power feed providing $4\times10^2$ MW in a $0.2\,\mu$s pulse. Stored energy per unit length would be under $40\,$J/m. Pulsed temperature rise in the secondary would be under $100\,$K, and under $40\,$K in the primary. For studies at lower power, a low-voltage 5 kW tube could drive the same linac to 3-MeV. The challenge of designing such a primary cavity lies in the problem of good coupling to the secondary line, so as to maintain the short discharge time-scale, equivalent to an external $Q$ after switch closure of $Q_e \approx 10^2$. We conclude that experimental and theoretical research into active, overmoded, mm-wave circuits[35] and photo-conductive switching[36] holds great promise for compact accelerators.

## ACKNOWLEDGMENTS

We are indebted to numerous co-workers at SLAC and elsewhere for helpful conversations, collaborations, and insights: Ping J. Chou, Marc Hill, Xintian E. Lin, Albert Menegat, Dennis T. Palmer, David P. Pritzkau, Robert H. Siemann, and Perry B. Wilson. We thank Angie Seymour for her continual support. Work was supported by U.S. Department of Energy, Contract DE-AC03-76SF00515.

## REFERENCES


[1] Robert N. Cahn and Gerson Goldhaber, *The Experimental Foundations of Particle Physics* (Cambridge University Press, Cambridge, 1989).

[2] *Proceedings of the 1996 DPB/DPF Workshop on New Directions for High Energy Physics* (AIP, New York, 1997).

[3] R. B. Palmer, *Ann. Rev. Nucl. Part. Sci.* **40** (1990) pp. 529-592.

[4] J. T. Seeman, *Ann. Rev. Nucl. Part. Sci.* **41** (1991) pp. 389-428.

[5] J. W. Wang and G. A. Loew, in *Frontiers of Accelerator Technology*, edited by S.I. Kurokawa, M. Month, S. Turner (World Scientific, Singapore, 1999).

[6] D. Pritzkau, A. Menegat, R.H. Siemann, T.G. Lee, and D.U.L. Yu, *Proceedings of the 1997 IEEE Particle Accelerator Conference* (IEEE, Piscataway, 1998), edited by M. Comyn, M.K. Craddock, M. Reiser, J. Thomson, pp. 3036-3038.

[7] T. Katsouleas, in *Advanced Accelerator Concepts*, AIP Proc. **398** (AIP, New York, 1997) pp. 175-180.

[8] D. H. Whittum, in *Frontiers of Accelerator Technology*, edited by S.I. Kurokawa, M. Month, S. Turner (World Scientific, Singapore, 1999).

[9] E. L. Ginzton, W. W. Hansen, and W. R. Kennedy, *Rev. Sci. Instrum.* **19** (1948) pp. 89-108.

[10] W.W. Hansen, *J. Appl. Phys.* **9** (1938) pp. 654-663.

[11] M. Chodorow, E. L. Ginzton, W. W. Hansen, R. L. Kyhl, R. B. Neal, W. K. H. Panofsky and The Staff, *Rev. Sci. Instrum.* **26** (1955) pp. 134-204.

[12] *The Stanford Two-Mile Accelerator*, R.B. Neal, editor (W.A. Benjamin, New York, 1968).

[13] *International Linear Collider Technical Review Committee Report*, edited by G. A. Loew and T. Weiland (SLAC, Stanford, 1995) SLAC-R-95-471.

[14] A. M. Sessler, D. H. Whittum, J. S. Wurtele, W. M. Sharp, and M. A. Makowski, *Nucl. Instrum. Methods* **A 306** (1991) pp. 592-605.

[15] F. Zimmermann and D. H. Whittum, *Int. J. Mod. Phys.* **A13** (1998) pp. 2525-2549.

[16] D.P. Pritzkau, 6 Sept. 1996 (unpublished).

[17] M. Abramowitz and I. A. Stegun, *Handbook of Mathematical Functions* (Dover, New York, 1965).

[18] D. E. Nagle, E. A. Knapp, and B. C. Knapp, *Rev. Sci. Instrum.* **38** (1967) pp. 1583 - 1587.

[19] For comparison, the Stanford Linear Collider consumed about 50 MW at 120 Hz, and the affordable operation schedule was affected by the corresponding operating cost.

[20] W. Bruns, *IEEE Trans. Mag.* **32** (1996) pp. 1453-1456.

[21] *Handbook of Industrial Diamonds and Diamond Thin Films*, Mark A. Prelas, Galina Popovici, and Louis K. Bigelow, eds. (Marcel Dekker, New York, 1998) pp. 147-192.

[22] *Diamond: Electronic Properties and Applications,* Lawrence S. Pan and Don R. Kania, eds. (Kluwer, Boston, 1995) p. 254.

[23] Manfred Thumm, *International Journal of Infrared and Millimeter Waves*, **19** (1998) pp. 3-14.

[24] L. S. Pan, *et al.*, Materials Research Society Symposium **302** (1993) pp. 299-304.

[25] P.-T. Ho, C.H. Lee, J.C. Stephenson, and R.R. Cavanagh, *Opt. Commun.* **46** (1983) pp. 202-204.

[26] W.K.H. Panofsky and W.A. Wenzel, *Rev. Sci. Instr.* **27** (1956) p. 967.

[27] H. Henke, AIP Conf. Proc. **398** (AIP, New York, 1997) pp. 485-500.

[28] D. R. Smith, Derun Li, D. C. Vier, N. Kroll, and S. Schultz, *Advanced Accelerator Concepts*, AIP Conf. Proc. **398** (AIP, New York, 1997) pp. 518-527.

[29] P.J. Chou, G.B. Bowden, M.R. Copeland, A. Menegat, R.H. Siemann and H. Henke, *Proceedings of the 1997 IEEE Particle Accelerator Conference,* edited by M. Comyn, M.K. Craddock, M. Reiser, J. Thomson (IEEE, Piscataway, 1998) pp. 464-466.

[30] P.J. Chou, G.B. Bowden, M.R. Copeland, A. Farvid, R.E. Kirby, A. Menegat, C. Pearson, L. Shere, R.H. Siemann, J.E. Spencer, and D.H. Whittum, *Advanced Accelerator Concepts*, AIP Conf. Proc. **398** (AIP, New York, 1997) pp. 501-517.

[31] S. M. Lidia, D. H. Whittum, and J. T. Donohue, *Proceedings of the 1997 IEEE Particle Accelerator Conference,* edited by M. Comyn, M.K. Craddock, M. Reiser, J. Thomson (IEEE, Piscataway, 1998) pp. 900-902.

[32] Z. D. Farkas, H. A. Hogg, G. A. Loew and P. B. Wilson, *IX Internat'l Conference on High Energy Accelerators* (SLAC, Stanford, 1974) p. 576.

[33] S. G. Tantawi, R. D. Ruth, A. E. Vlieks, and M. Zolotorev, *Advanced Accelerator Concepts*, AIP Proc. **398** (AIP, New York, 1997) pp. 813-821.

[34] S. L. Allen, C.J. Lasnier, B. Felker, M. Fenstermacher, S.W. Ferguson, S. Fields, E.B. Hooper, S. Hulsey, M. Makowski, J. Moller, W. Meyer, D. Petersen, E.T. Scharlemann, B. Stallard, R. Wood, *Proceedings of the 1993 Particle Accelerator Conference* (Washington, D.C., 1993) pp. 1551-1553.

[35] M. I. Petelin, A. L. Vikharev and J. L. Hirshfield, *Advanced Accelerator Concepts*, AIP Proc. **398** (AIP, New York, 1997) pp. 822-831.

[36] C. Bamber, W. Donaldson, E. Lincke, and A. C. Melissinos, *Nucl. Instrum. Meth.* **A 327** (1993) pp. 227-252.

**FIGURE 1.** Illustration of the conventional travelling wave accelerator concept, employing a linear array of circular resonant cavities, coupled by means of the beam passing aperture, and powered by means of a waveguide feed to the first cell.

**FIGURE 2.** Illustrating ideas one may have for avoiding the pulsed heating limits inherent in the conventional travelling wave accelerator illustrated in **(a).** In **(b)** we consider employing a much shorter electromagnetic ("RF") pulse and a shorter structure, but require multiple beam lines to recoup efficiency. In **(c)**, realizing that multiple beamlines will be required if exposure time is short, we carry (b) to its logical extreme, envisioning a matrix of accelerating cells.

**FIGURE 3.** We reduce Fig. 2(c) to its simplest form, and contemplate the problem of non-parallel signal and beam transmission channels.

**FIGURE 4.** Illustration of the bunch and signal ("RF") schedules for **(a)** a conventional travelling-wave accelerator, and **(b)** the accelerator we propose to analyze, with beams in parallel channels. For multibunch operation with short exposure time of copper to accelerating fields, bunches must be propagated in parallel. The resulting transverse extent for the matrix of accelerating cells then favors a short operating wavelength, of order millimeters or less, in order to fit the device on a substrate a few inches in width.

**FIGURE 5. (a)** Matrix accelerator during charge-up. **(b)** After closing of the switches the signal propagates down each secondary line, and electron bunches arrive in parallel to be accelerated.

**FIGURE 6.** A perspective view of the physical layout corresponding to Fig. 5.

**FIGURE 7.** This is a top view of Fig. 6. We will analyze an implementation of the desired circuit behavior seen in Fig. 5, in rectangular guide employing a switch configured from an H-plane tee with an embedded photoconductor. We select coordinates such that the signal propagates down the secondary in the *x*-direction, and the electron beams propagate in the *z*-direction.

**FIGURE 8.** In the first approximation, the cell geometries of both the primary and secondary lines are rectangular pillboxes, with excitations corresponding to the $TE_{10m}$ mode. For the primary cell, $m$>>1, while for the secondary $m$=1. Thus $w_1 >> w_2$.

**FIGURE 9.** Depicted are voltage waveforms versus normalized time, for an initially square pulse of unit amplitude, after *first-order* dispersion in a transmission line, for several values of normalized pulse length, **(a)** $\hat{T}_p = 1.0$, **(b)** $\hat{T}_p = 2.0$, **(c)** $\hat{T}_p = 3.0$, and **(d)** $\hat{T}_p = 100$.

**FIGURE 10.** Depicted are voltage waveforms versus normalized time, for an initially square pulse of unit amplitude, after *second-order* dispersion dominated transport in a periodic line, for several values of normalized pulse length , **(a)** $\hat{T}_p = 2.0$, **(b)** $\hat{T}_p = 5.0$, **(c)** $\hat{T}_p = 10.0$, and **(d)** $\hat{T}_p = 100$.

**FIGURE 11.** We consider a discrete coupled-cavity simulation to model the discharge of the primary line into the secondary, and pulse propagation on the secondary line. This is Fig. 7 with the forward, reverse and cell voltages overlaid, and the switch replaced with straight waveguide. The output end (not shown) of the secondary line is assumed to be perfectly matched.

**FIGURE 12.** To illustrate the forward voltage employed for the coupled-cavity simulations, and typical waveforms for the reverse voltage, and the input coupler cell voltage.

**FIGURE 13.** Illustrating the voltage waveforms at cells 1, 33-35, and 48-50, on a constant-gradient line with $Q_w \approx 2700$, initial group velocity 0.174*c* and no beam-loading.

**FIGURE 14**. This plot illustrates the maximum (over time) of each cell voltage for different conditions. The uppermost curve corresponds to a lossless structure. ($Q_w \approx \infty$), while other curves correspond to $Q_w \approx 2700$. Also shown are for a constant-impedance (CZ) line and a constant-gradient (CG) line. The dashed curve corresponds to the constant-gradient line with 21.4% loading

over 50 beamlines.

**FIGURE 15.** Parameters characterizing the secondary line geometry are illustrated. The depth dimension *a* is into the page.

**FIGURE 16.** Secondary cell geometry employed in the electromagnetic field solver, cut at symmetry planes in *x* and *y*. Surfaces depicted correspond to the interior conducting boundaries.

**FIGURE 17.** Illustration of cell-geometry errors corresponding to **(a)** a 6.5 mil gap between coupling-irises and the cell floor, and **(b)** a $5\,\text{mil} \times 5\,\text{mil}$ corner post. As in Fig. 16, the cell geometry has been cut at symmetry planes in *x* and *y*.

**FIGURE 18.** A seven-cell section matched to WR10 input and output.

**FIGURE 19.** Moduli of the S-matrix elements **(a)** $S_{11}$ and **(b)** $S_{21}$ as computed with GdfidL for the seven cell test block of Fig. 18.

**FIGURE 20.** S-matrix elements **(a)** $S_{11}$ and **(b)** $S_{21}$ as computed with the coupled-cavity model.

**FIGURE 21.** Illustrating the H-plane tee geometry employed for the switch. The electric field points into the plane. The depth into the plane is $b = 0.05"$, the small dimension of WR10, and $a = 0.10"$ is the long dimension. The dashed lines define reference planes for the calculation.

**TABLE 1.** Three example designs corresponding to **(a)** negligible beam loading **(b)** conservative estimate of loading with $N_2 q_b \approx 3$ nC, and **(c)** low-group velocity and negligible beam loading.

| **Parameter** | **(a)** | **(b)** | **(c)** |
|---|---|---|---|
| $V_{g2}(0)$ | $0.174c$ | $0.174c$ | $0.123c$ |
| $N_2$ | 35 | 35 | 15 |
| $\Delta T$ | 126 K | 168 K | 126 K |
| $U_1$ | 88 mJ | 117 mJ | 62 mJ |
| $U_1 / L$ | 72 J/m | 96 J/m | 51 J/m |
| $\tau_1$ | 1.05 | 1.05 | 1.27 |
| $T_1$ | 18.2 ns | 18.2 ns | 22.1 ns |
| $P_1$ | $3.0\times10^2$ MW | $4.0\times10^2$ MW | $1.7\times10^2$ MW |
| $P_1 T_1$ | 5.5 J | 7.3 J | 3.8 J |
| $G_{\max}$ | 1.2 GeV/m | 1.4 GeV/m | 1.2 GeV/m |

**TABLE 2.** Dimensions for the idealized planar secondary cell, normalized to the free-space wavelength $\lambda \approx 3.28\,\text{mm}$.

| feature | notation | units of $\lambda$ | units of mm |
|---|---|---|---|
| cell period | $w_2$ | 0.831 | 2.73 |
| ...(coupling cells) | $w_{2c}$ | 0.864 | 2.83 |
| iris width | $t$ | 0.085 | 0.28 |
| ...(coupling irises) | $t_c$ | 0.077 | 0.25 |
| iris gap | $2d$ | 0.039 | 0.13 |
| ...(coupling irises) | $2d_c$ | 0.120 | 0.39 |
| transit length | $L$ | 0.391 | 1.28 |
| pipe diameter | $2R$ | 0.211 | 0.69 |
| depth | $a$ | 0.746 | 2.45 |

**TABLE 3.** Effect of errors in the major dimensions. Column (2) lists the error placed in the geometry as a percent of the nominal value (as listed in Table 2), and the absolute error in microns. Column (3) lists the resulting error in the mode frequency, as a percentage, and in absolute terms. The last column lists an estimate of the absolute dimensional tolerance in units of mil (0.001"=25.4 $\mu$m) corresponding to a frequency error of 0.27 GHz, obtained by scaling column (3) in inverse proportion to column (4).

| dimension | error(%) | error($\mu$m) | $\delta f$(%) | $\delta f$(GHz) | $\delta[R/Q]$(%) | $\delta Q_w$(%) | est.(mil) |
|---|---|---|---|---|---|---|---|
| $w_2$ | 1 | 27 | –0.55 | –0.50 | +0.3 | –0.4 | 0.5 |
| $t$ | 10 | 28 | -0.27 | -0.25 | +1.2 | –0.3 | 1.1 |
| $2d$ | 10 | 13 | +0.30 | +0.27 | -1.6 | +0.3 | 0.5 |
| $L$ | 10 | 128 | -0.48 | -0.44 | -1.5 | +4.7 | 3.0 |
| $2R$ | 10 | 69 | +0.29 | +0.26 | -3.5 | +0.5 | 2.7 |
| $a$ | 1 | 25 | -0.46 | -0.42 | +0.2 | +0.1 | 0.6 |

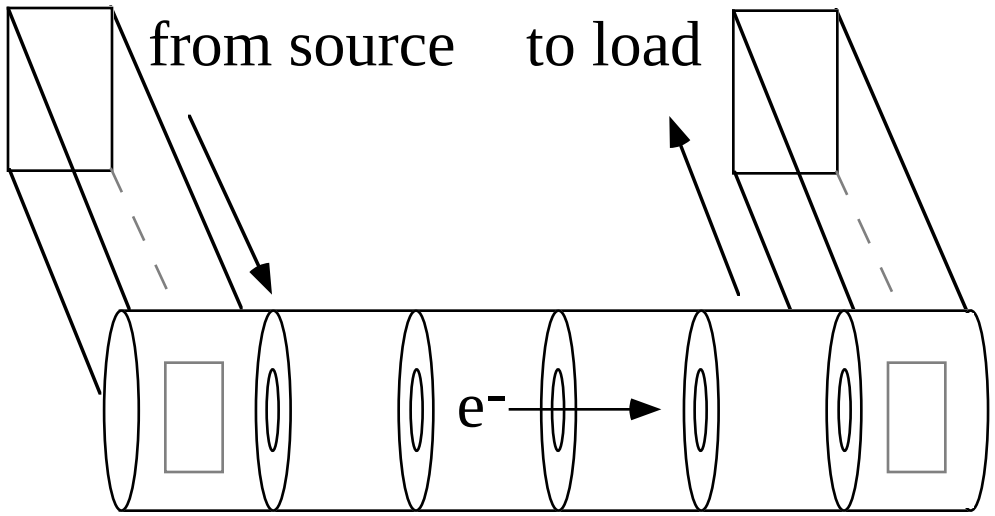


FIG. 1

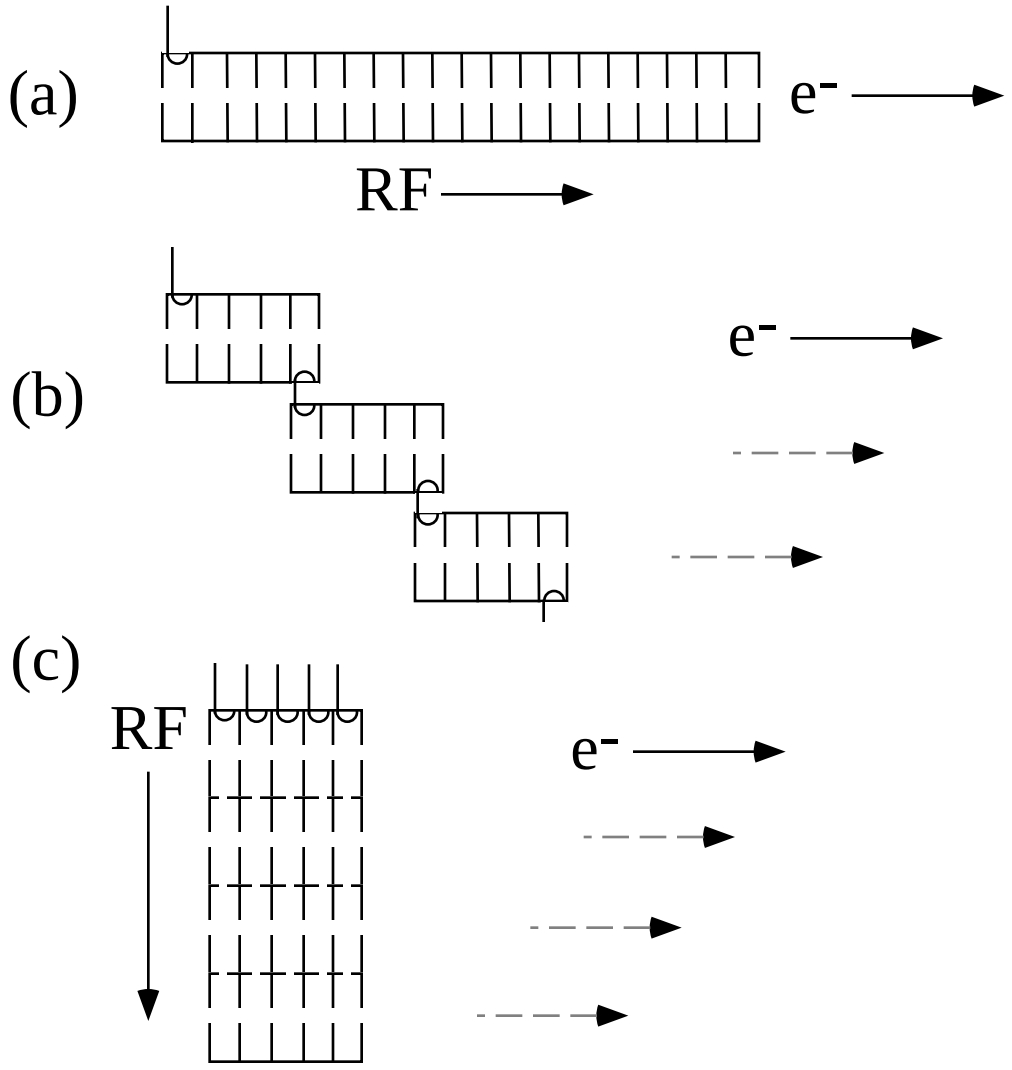


FIG. 2

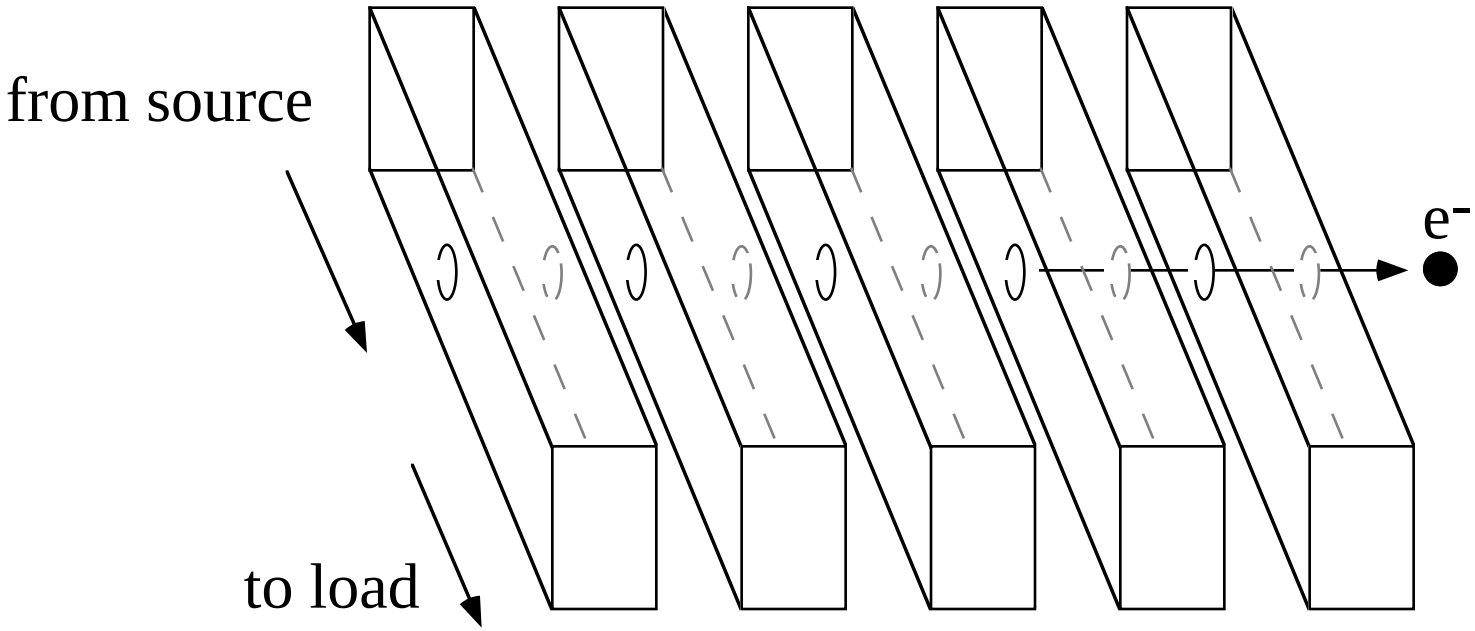


FIG. 3

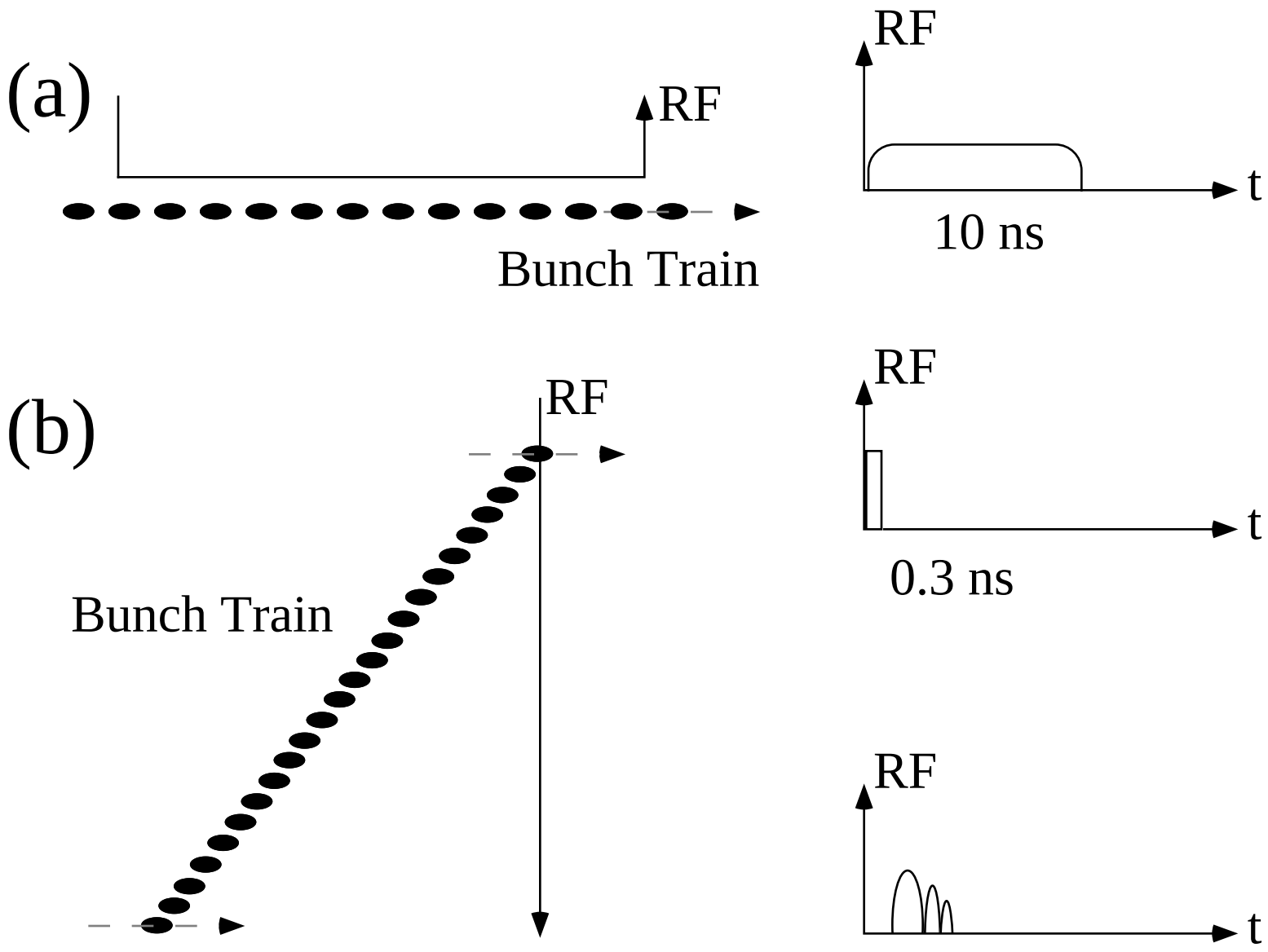


FIG. 4

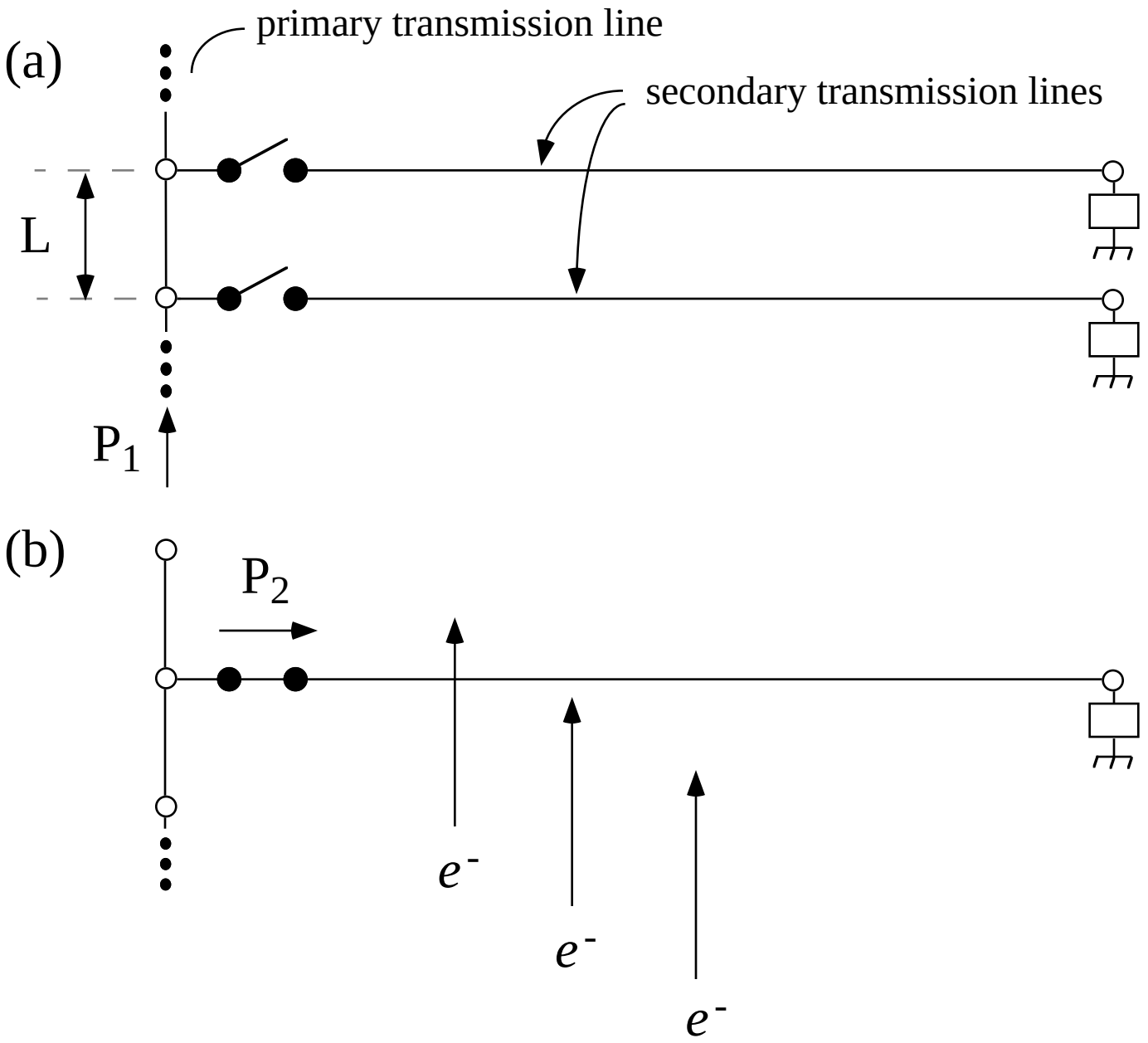
(a)
primary transmission line
secondary transmission lines
L
P1
(b)
P2
e-
e-
e-

FIG. 5

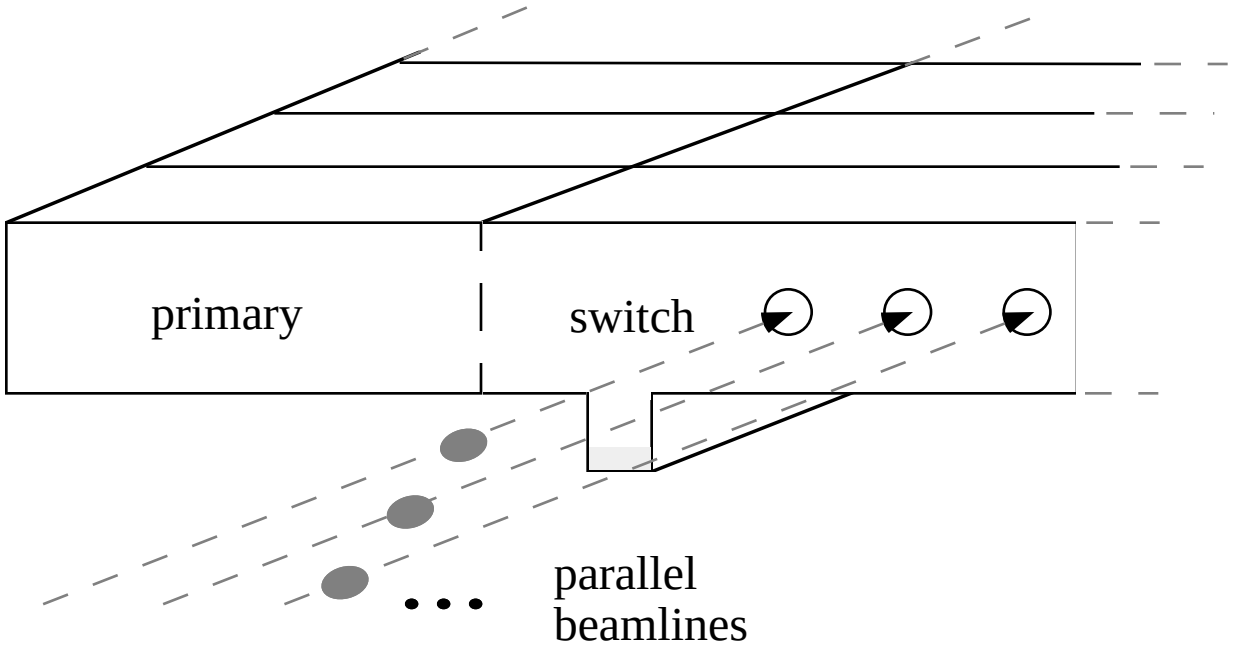


FIG. 6

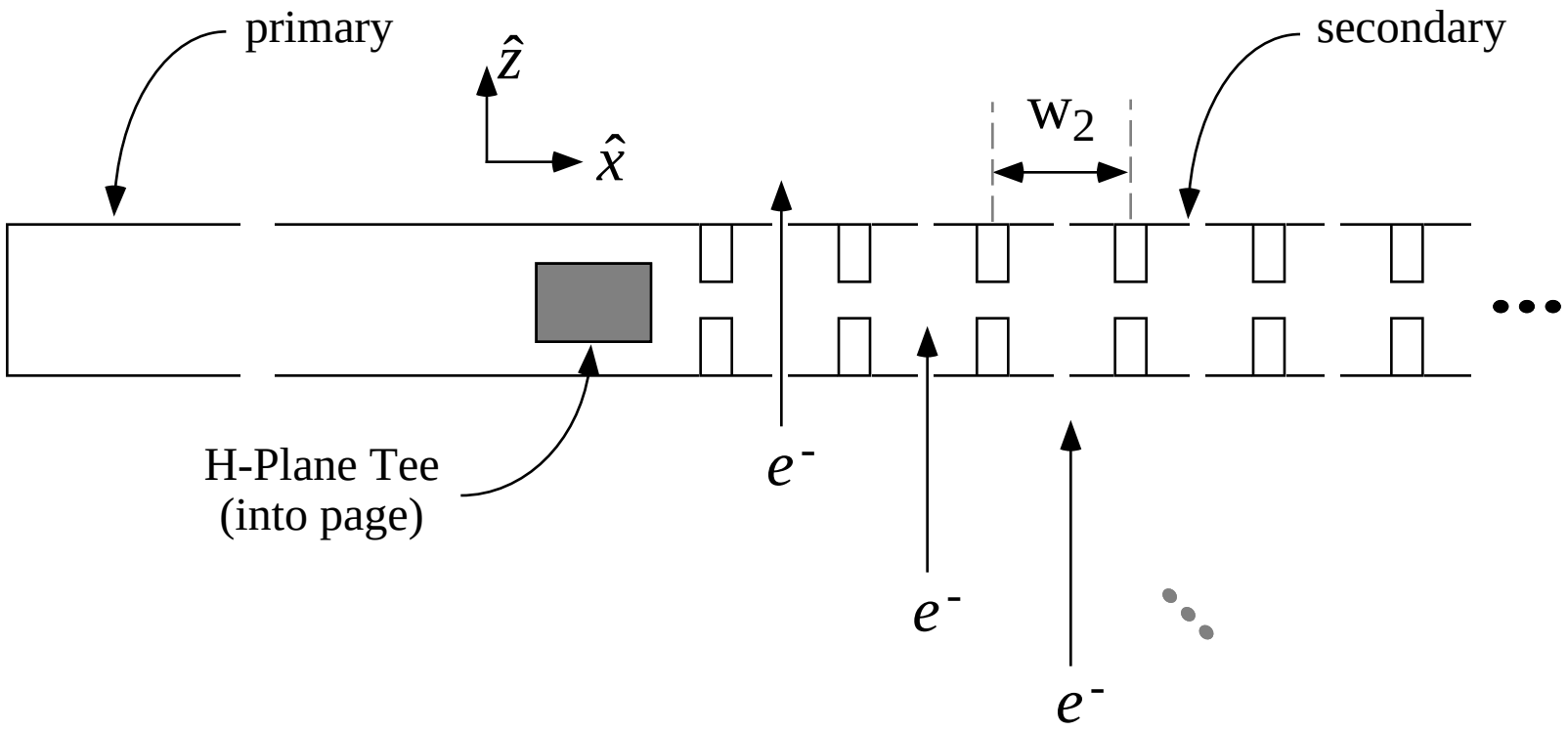


FIG. 7

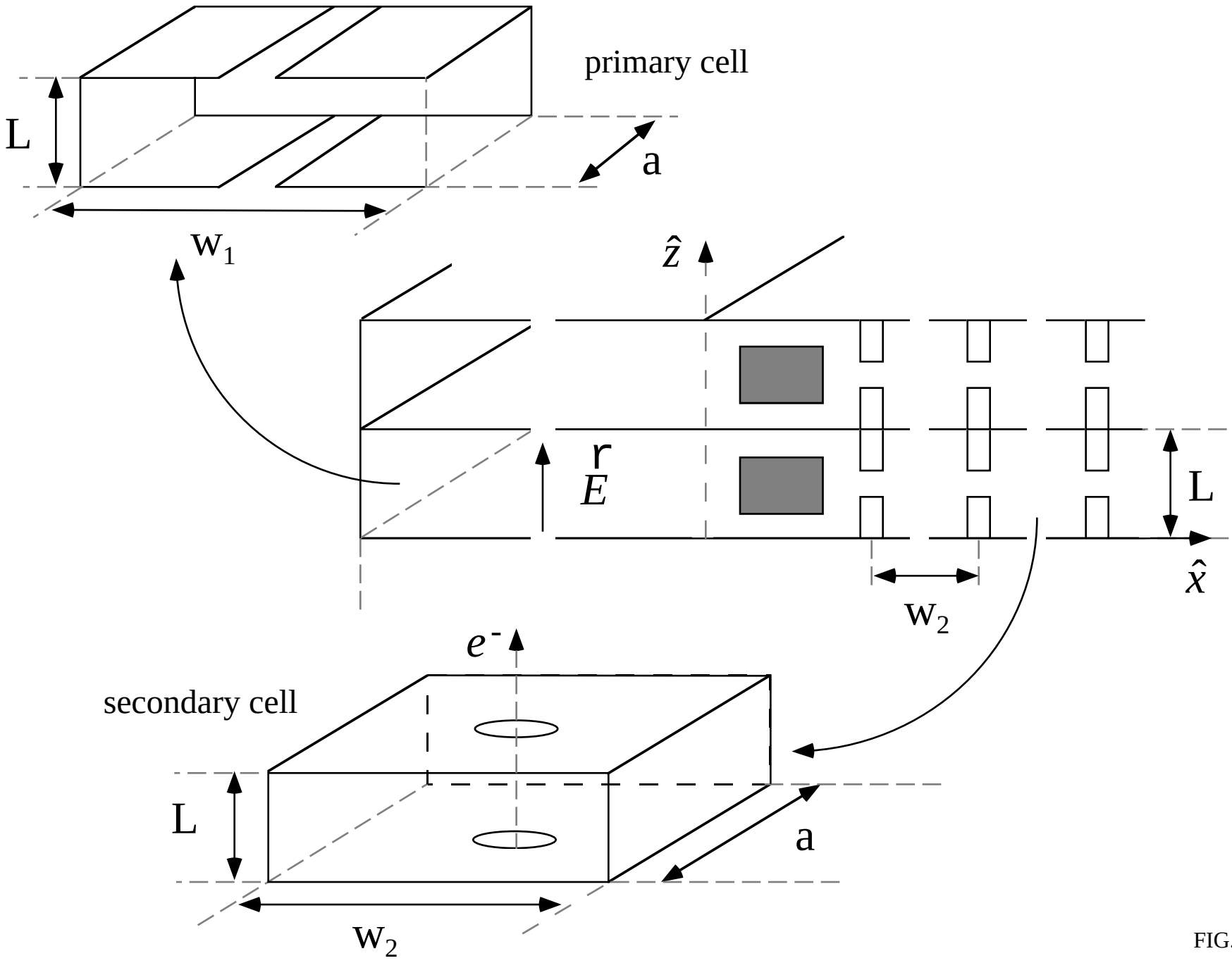


FIG.8

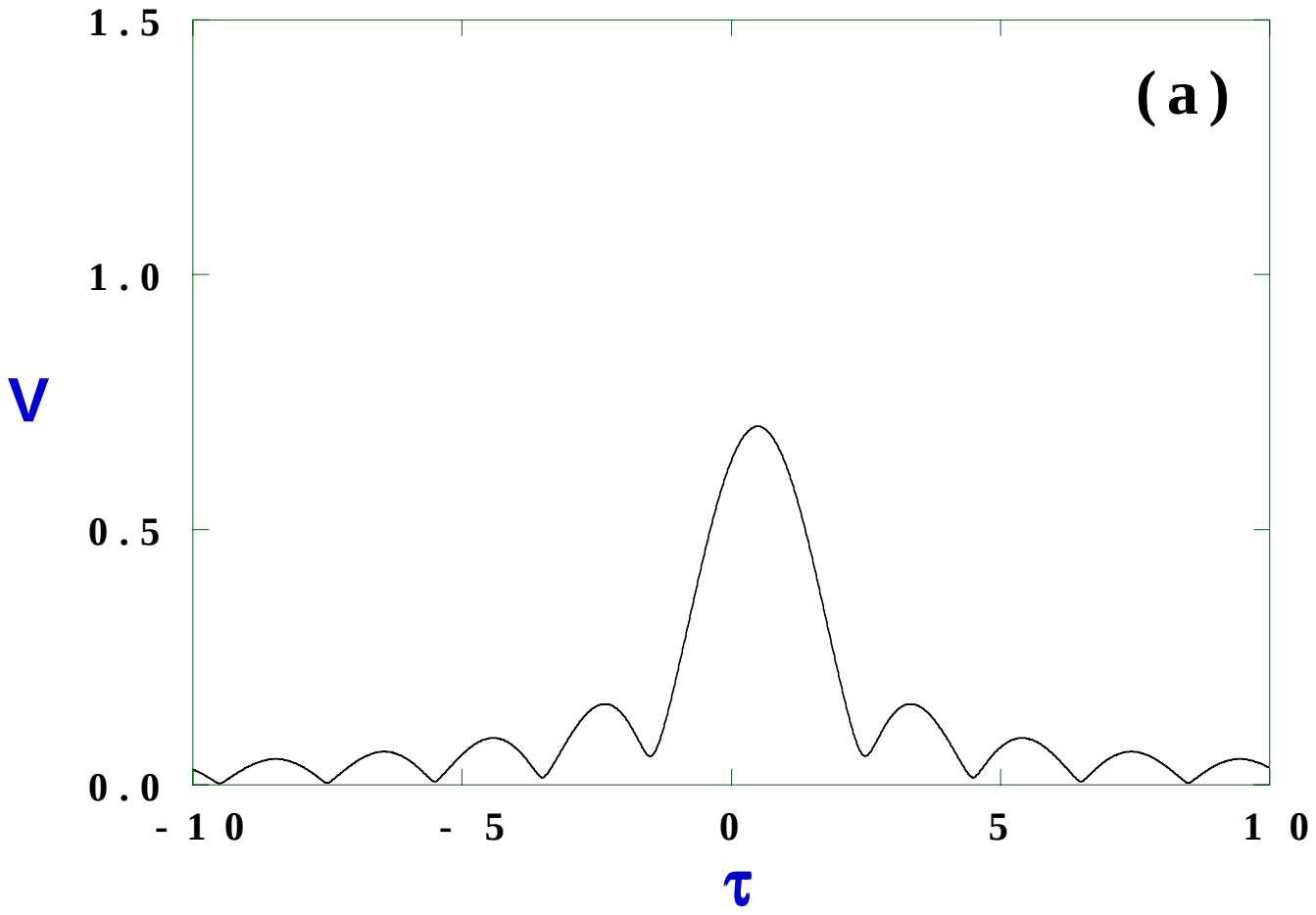


FIG. 9a

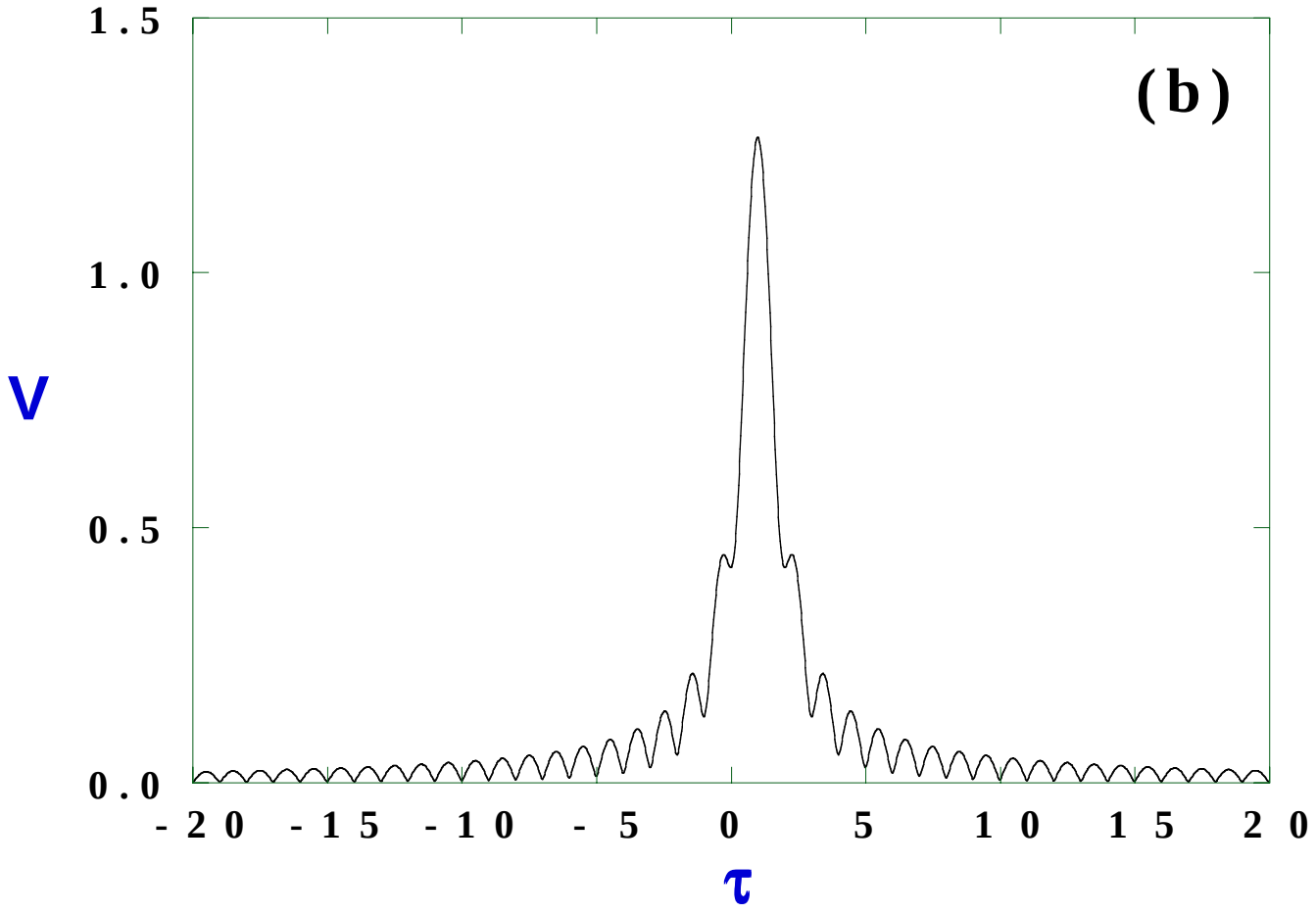


FIG. 9b

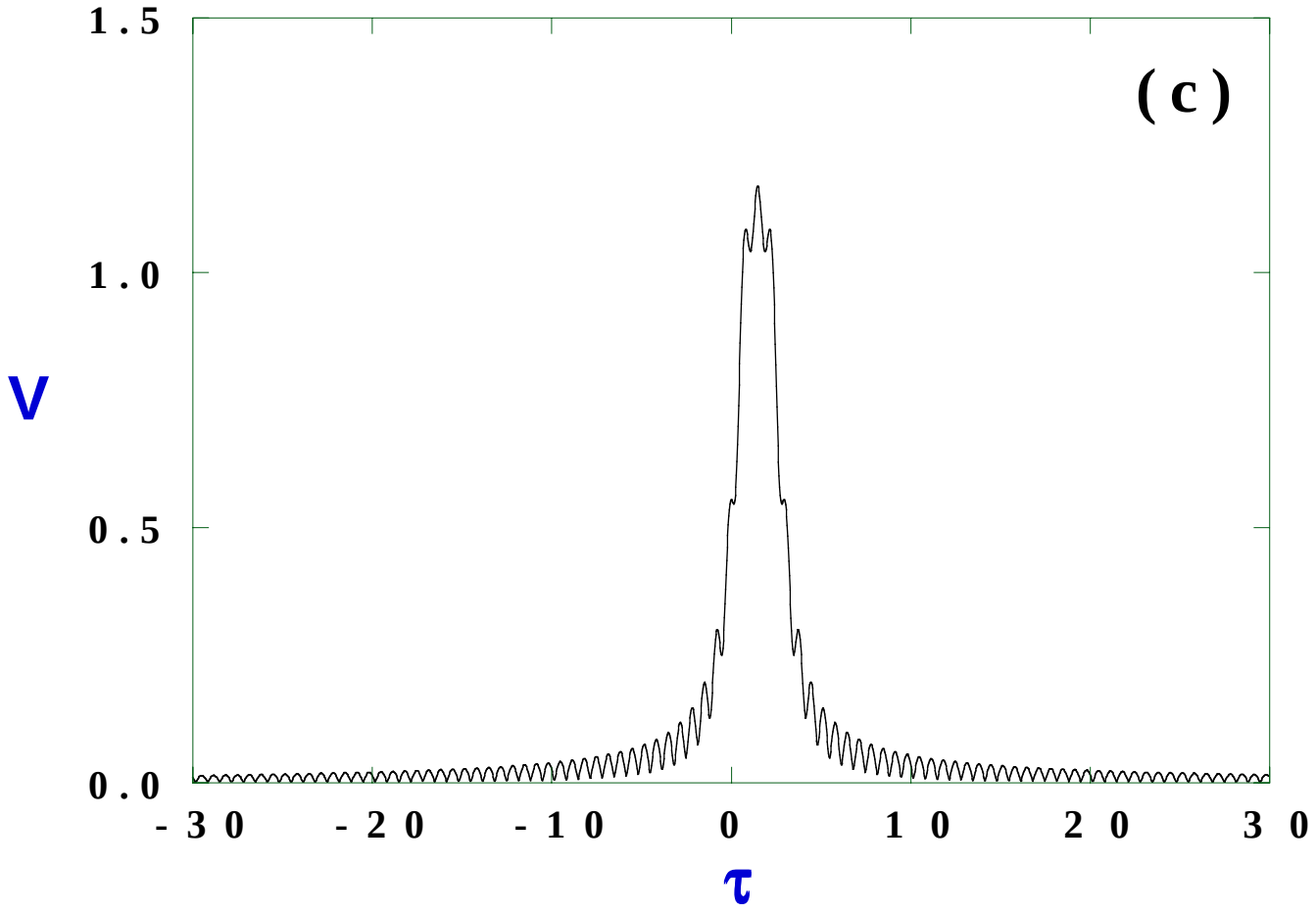


FIG. 9c

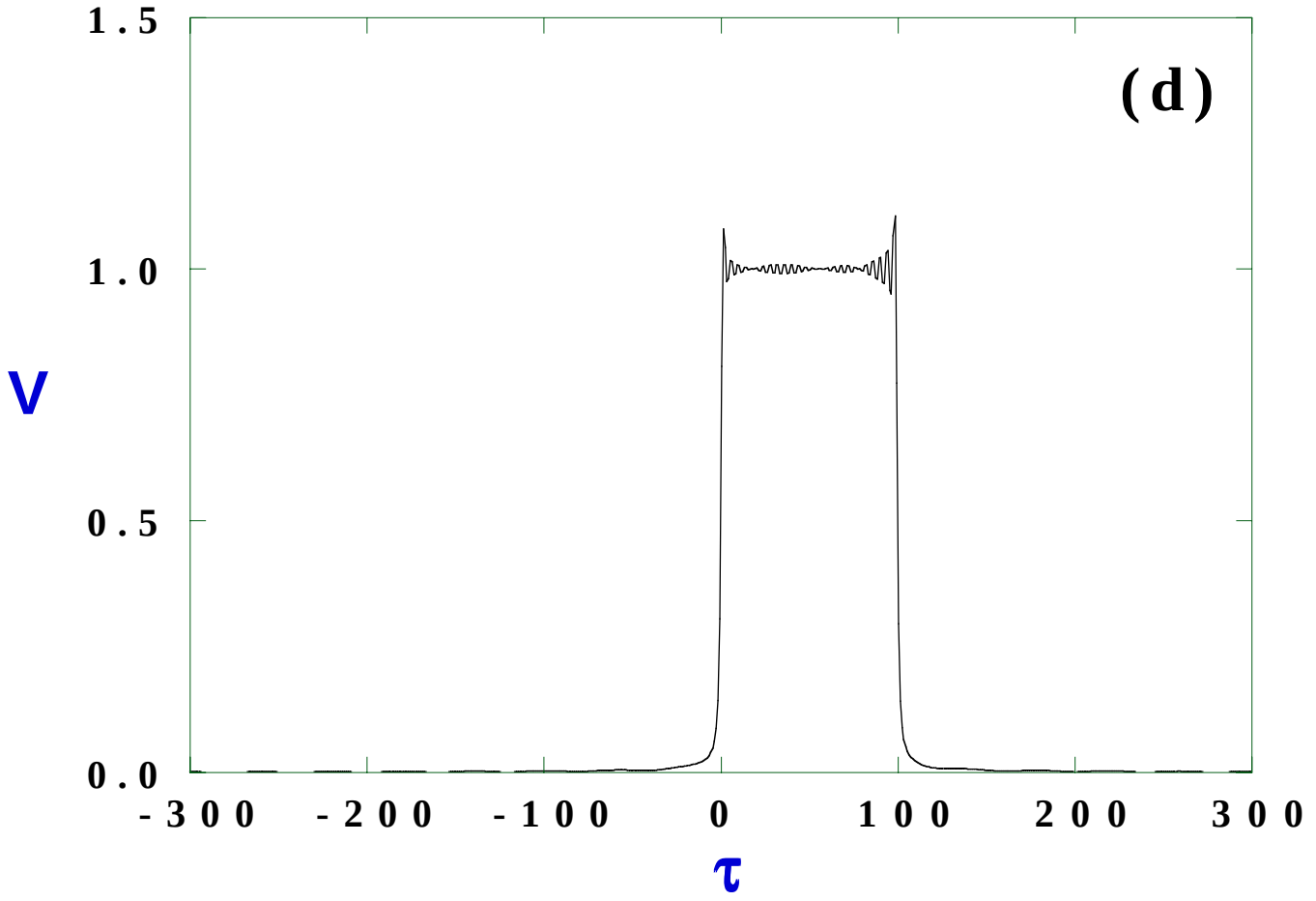


FIG. 9d

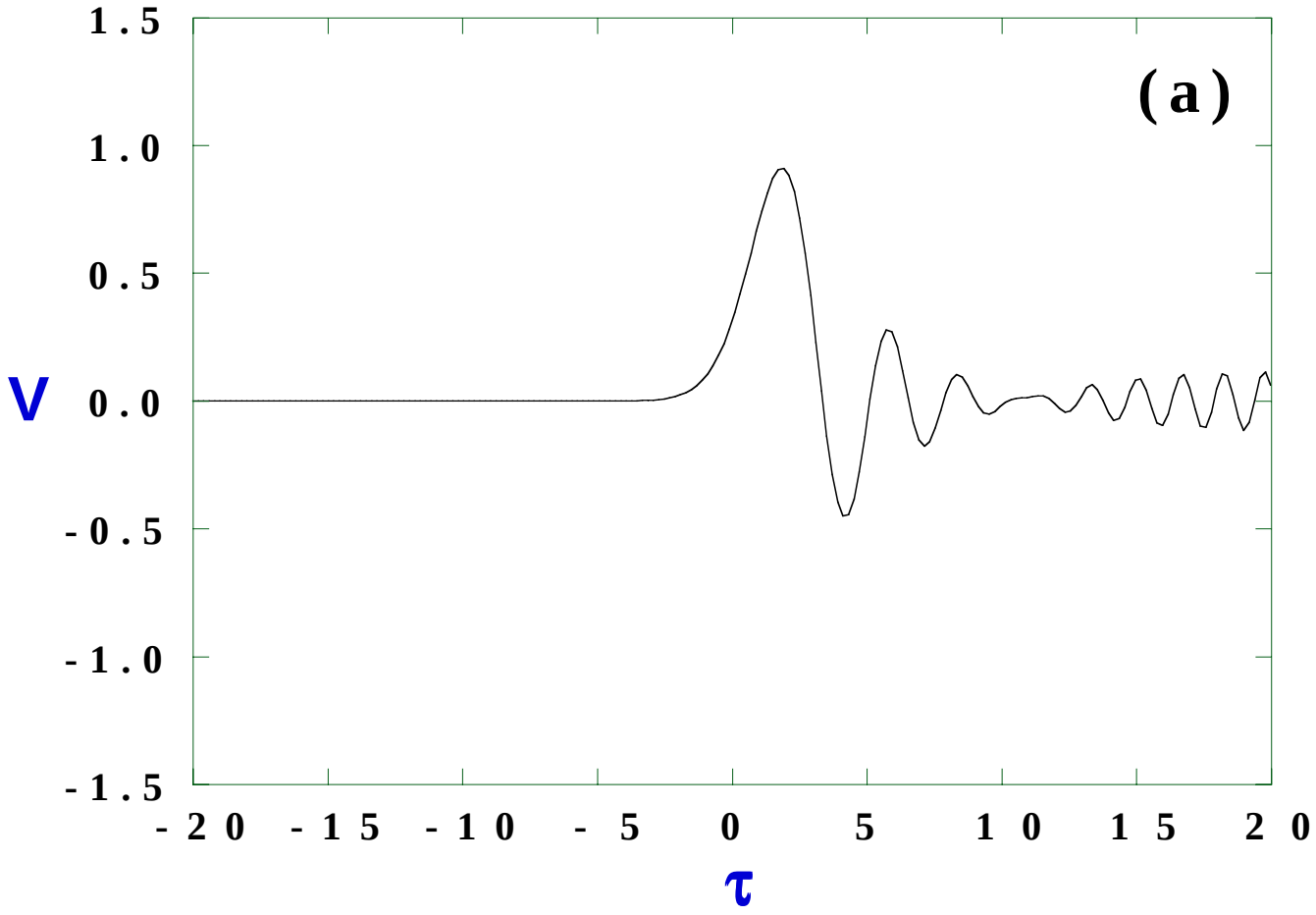


FIG. 10a

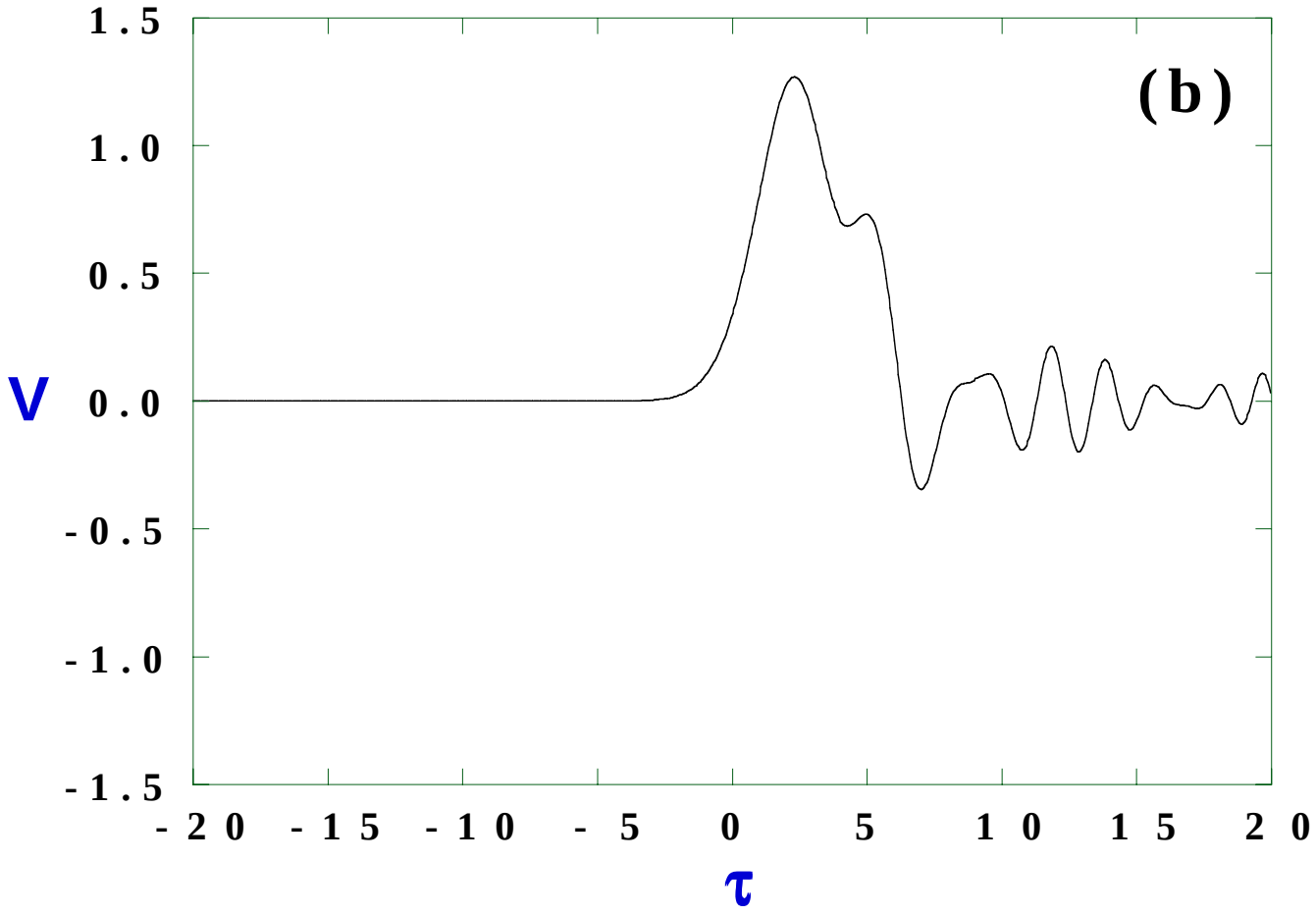


FIG. 10b

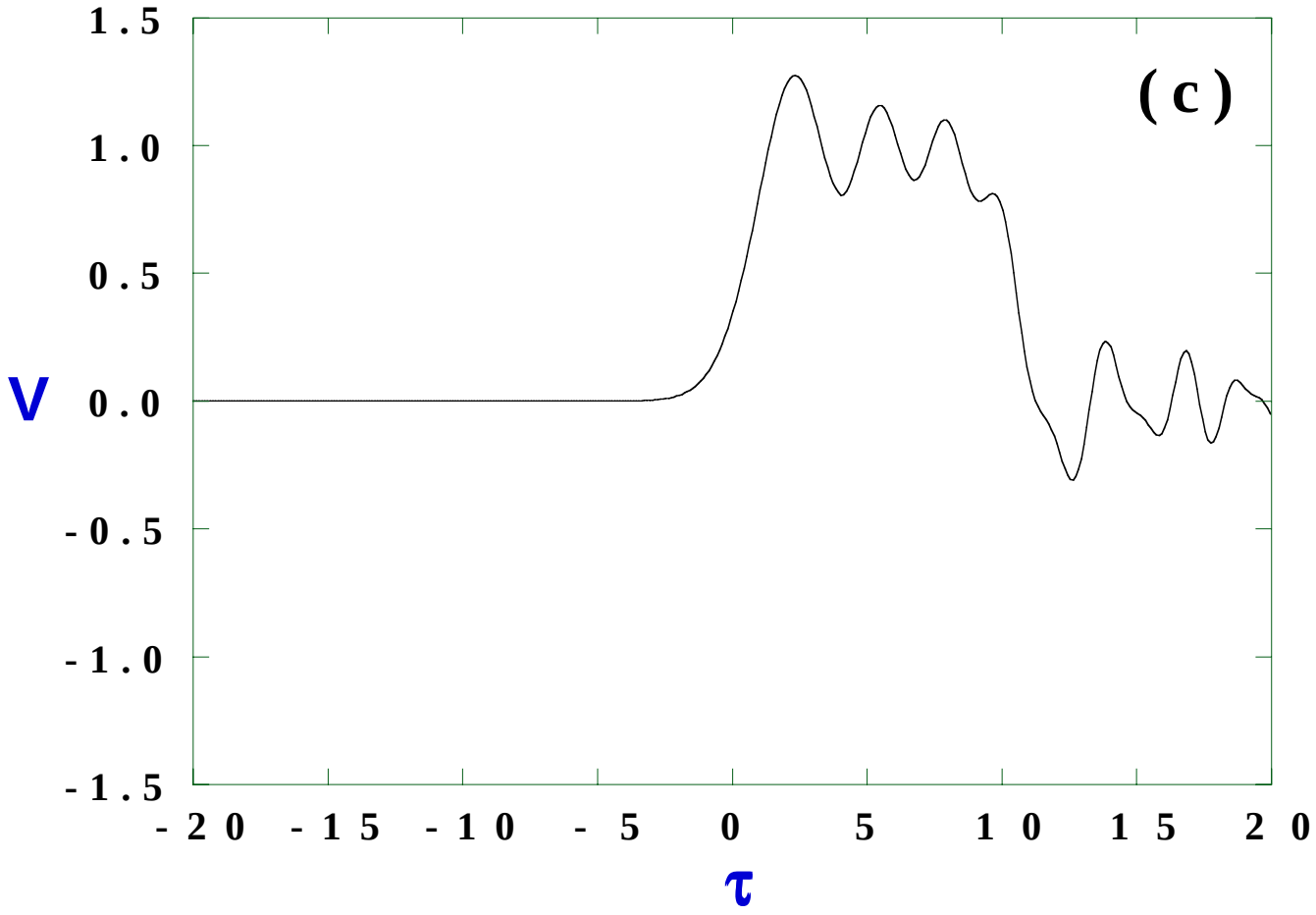


FIG. 10c

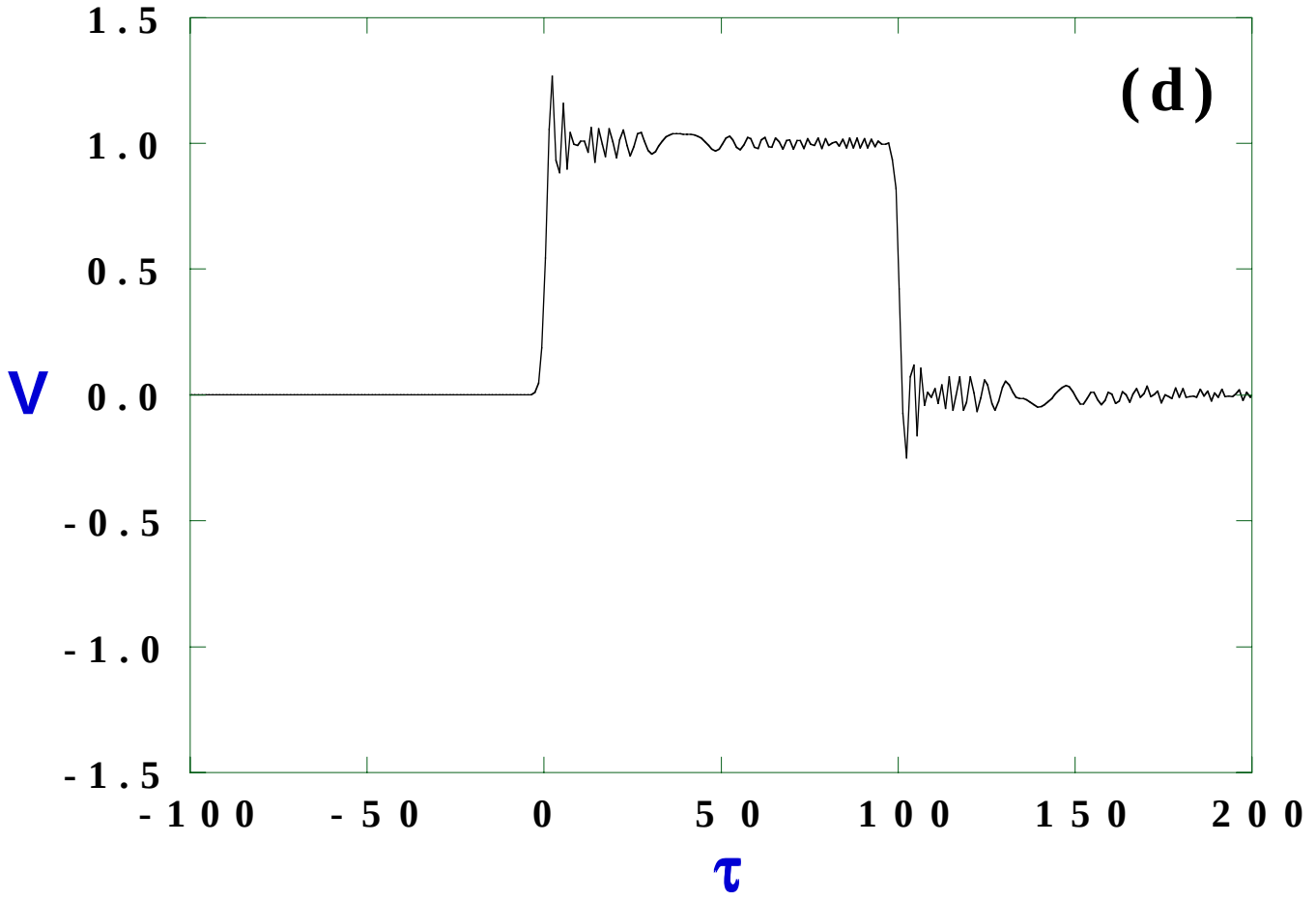


FIG. 10d

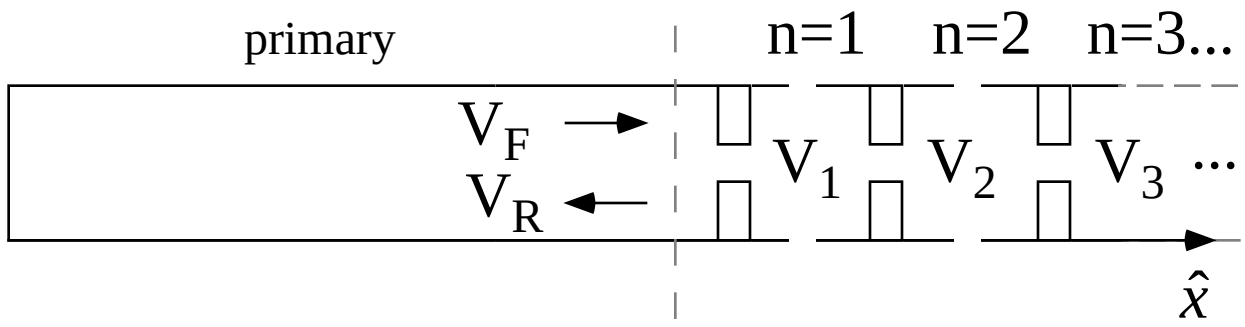


FIG.11

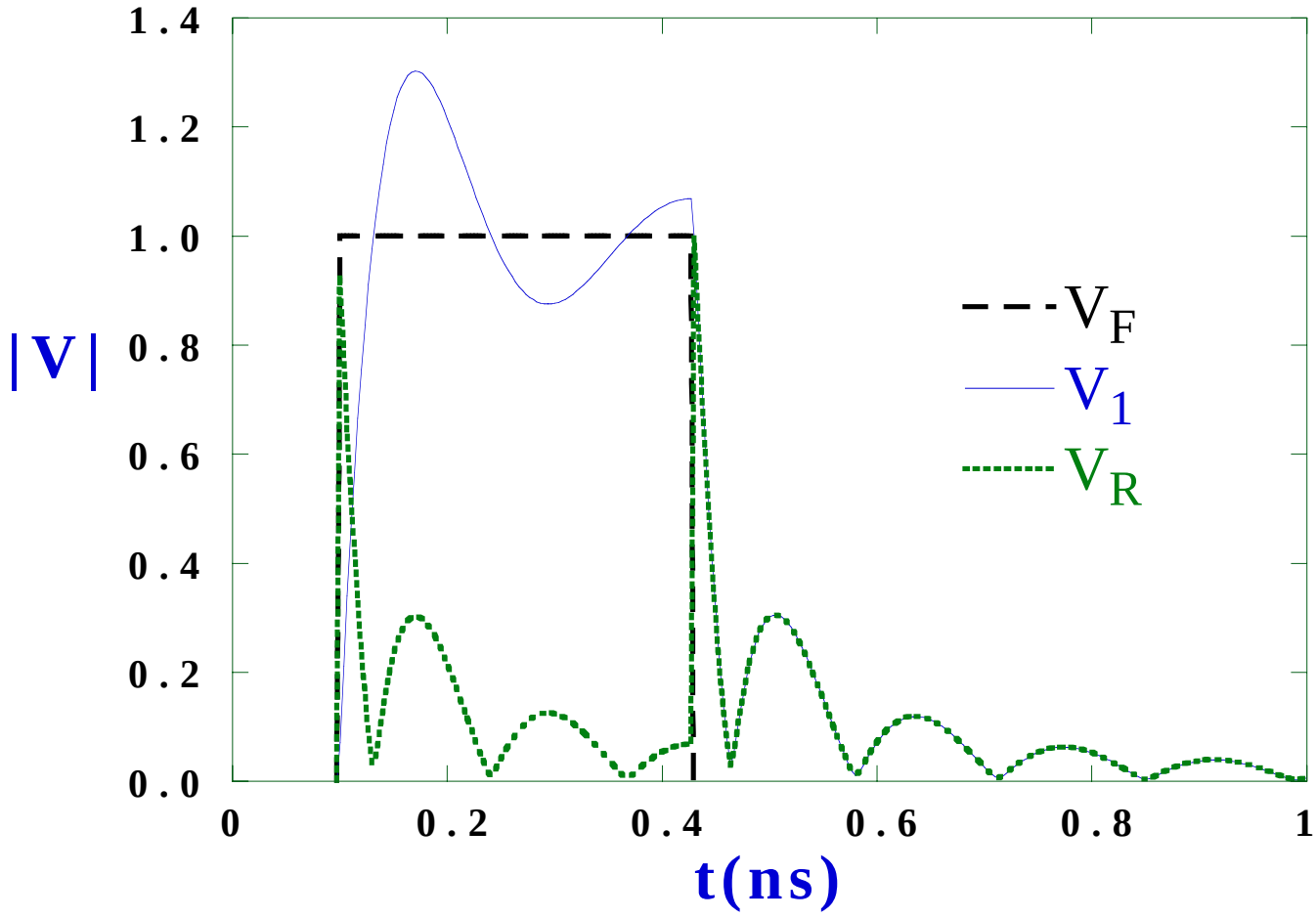


FIG. 12

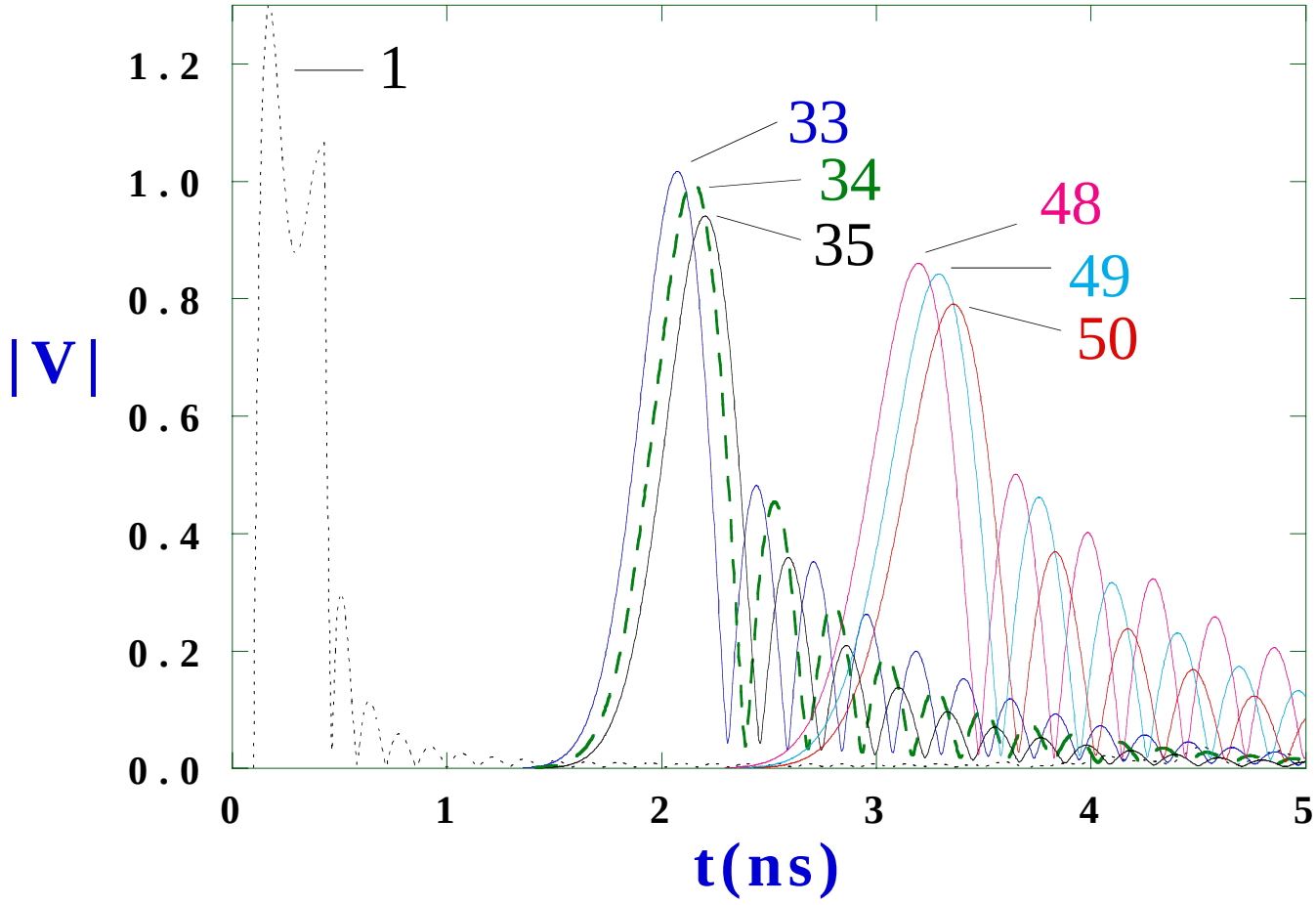


FIG. 13

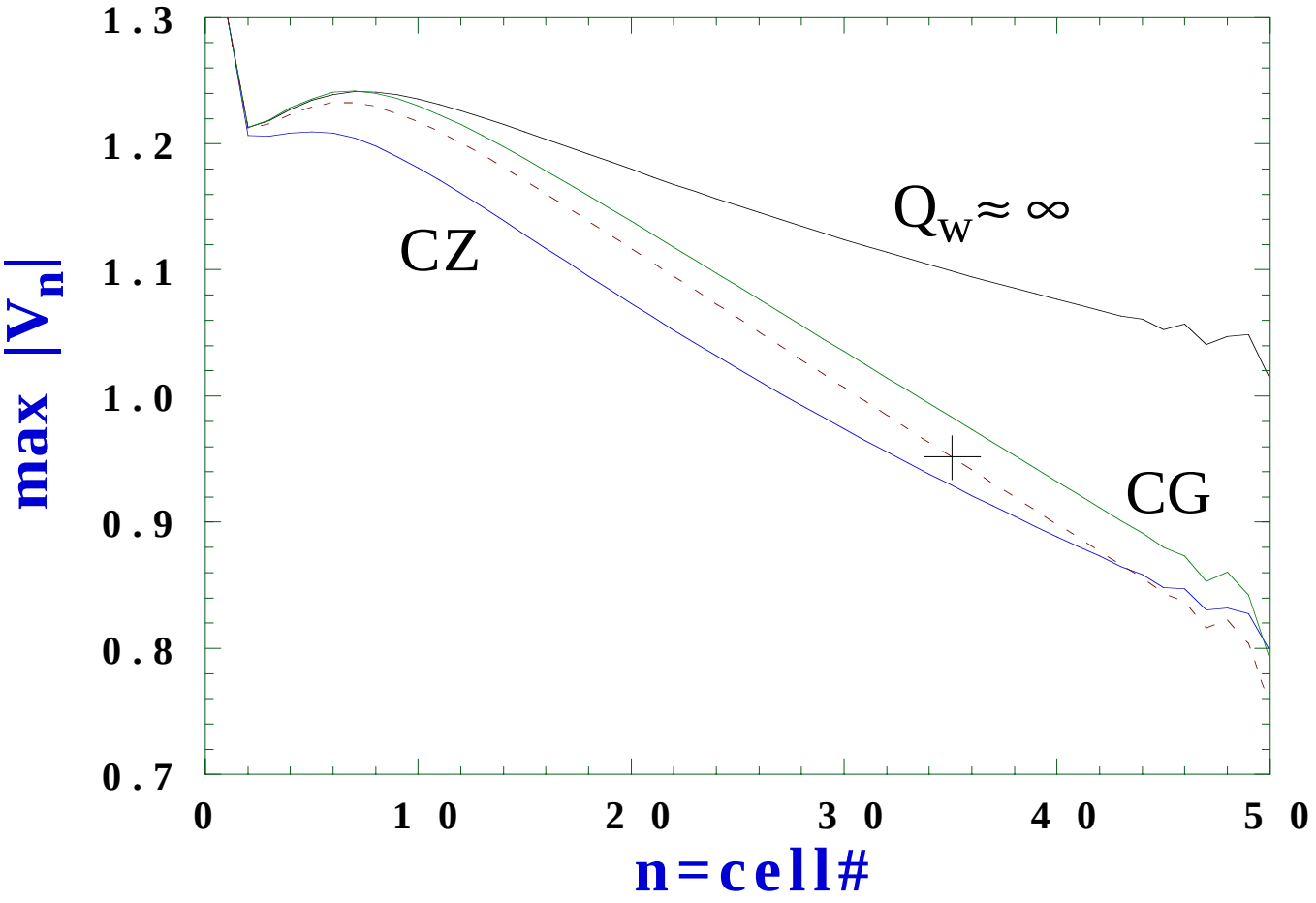


FIG. 14

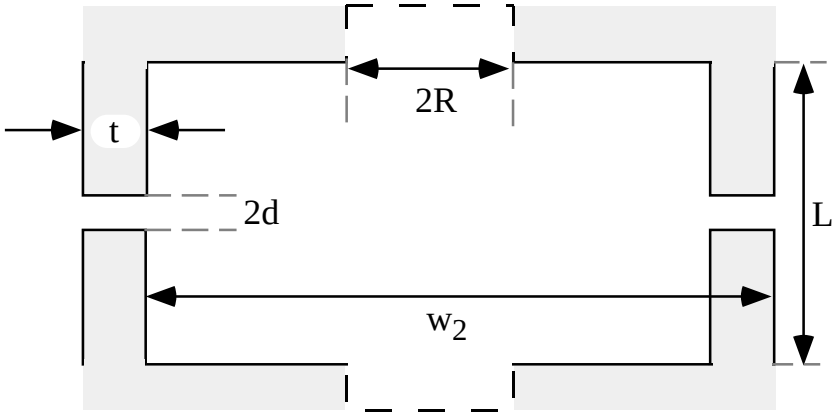


FIG.15

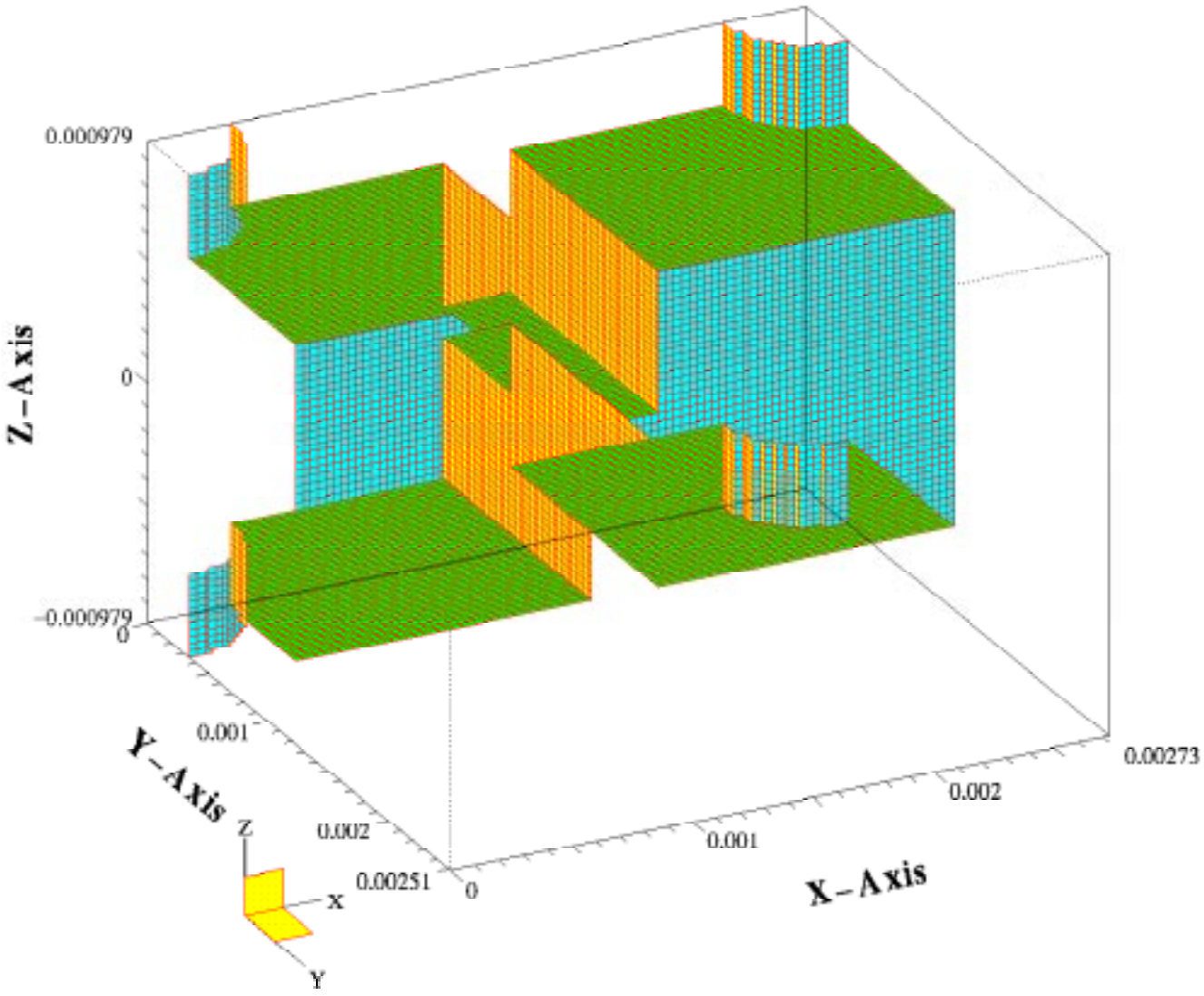
0.000979
0
-0.000979
Z-Axis
0
0.001
0.002
0.00251
Y-Axis
Z
X
Y
0
0.001
0.002
0.00273
X-Axis

FIG. 16

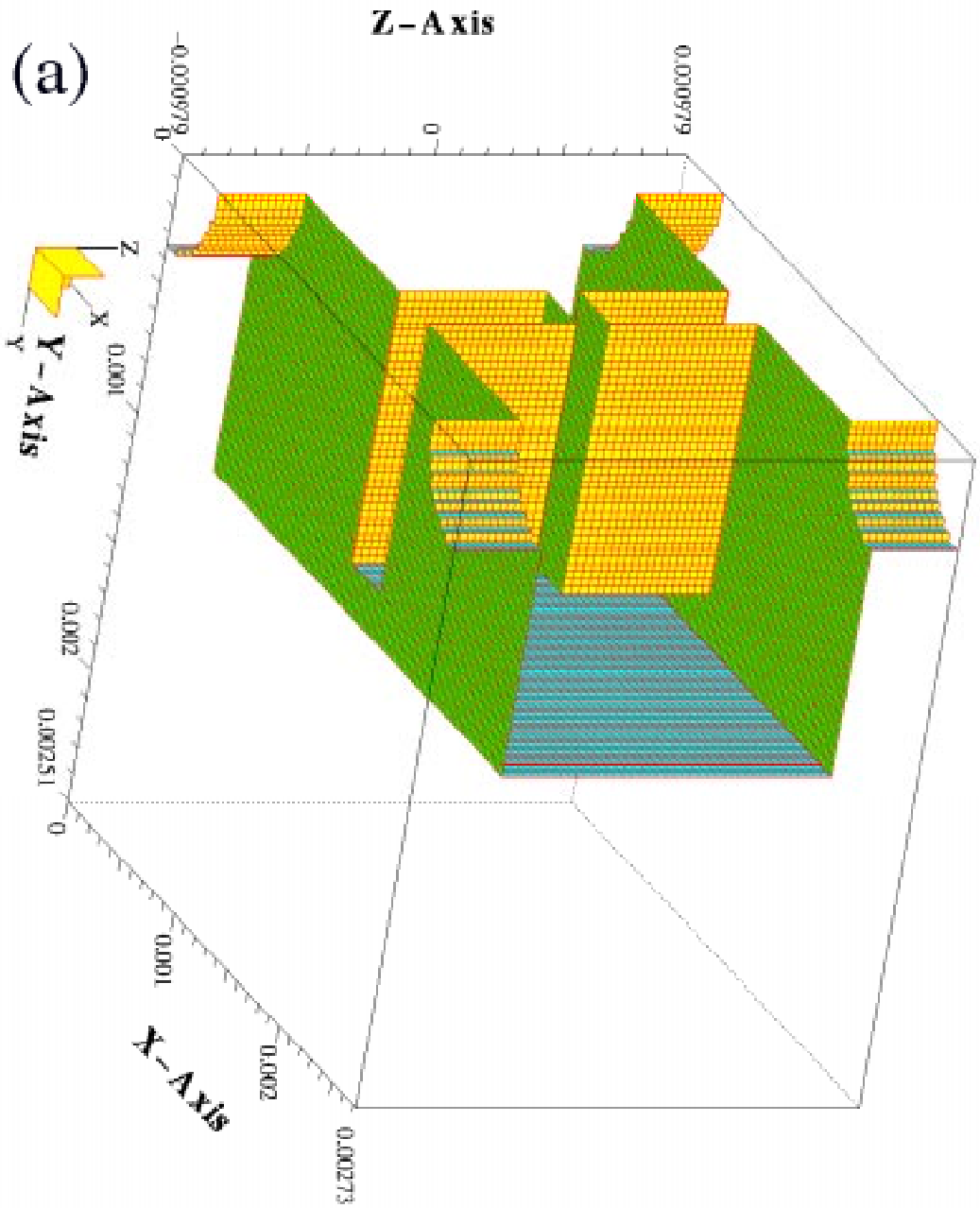
(a)
Z – Axis
-0.000979
0
0.000979
Z
X
Y
Y – Axis
0.001
0.002
0.00251
0
0.001
0.002
X – Axis
0.00273

FIG. 17(a)

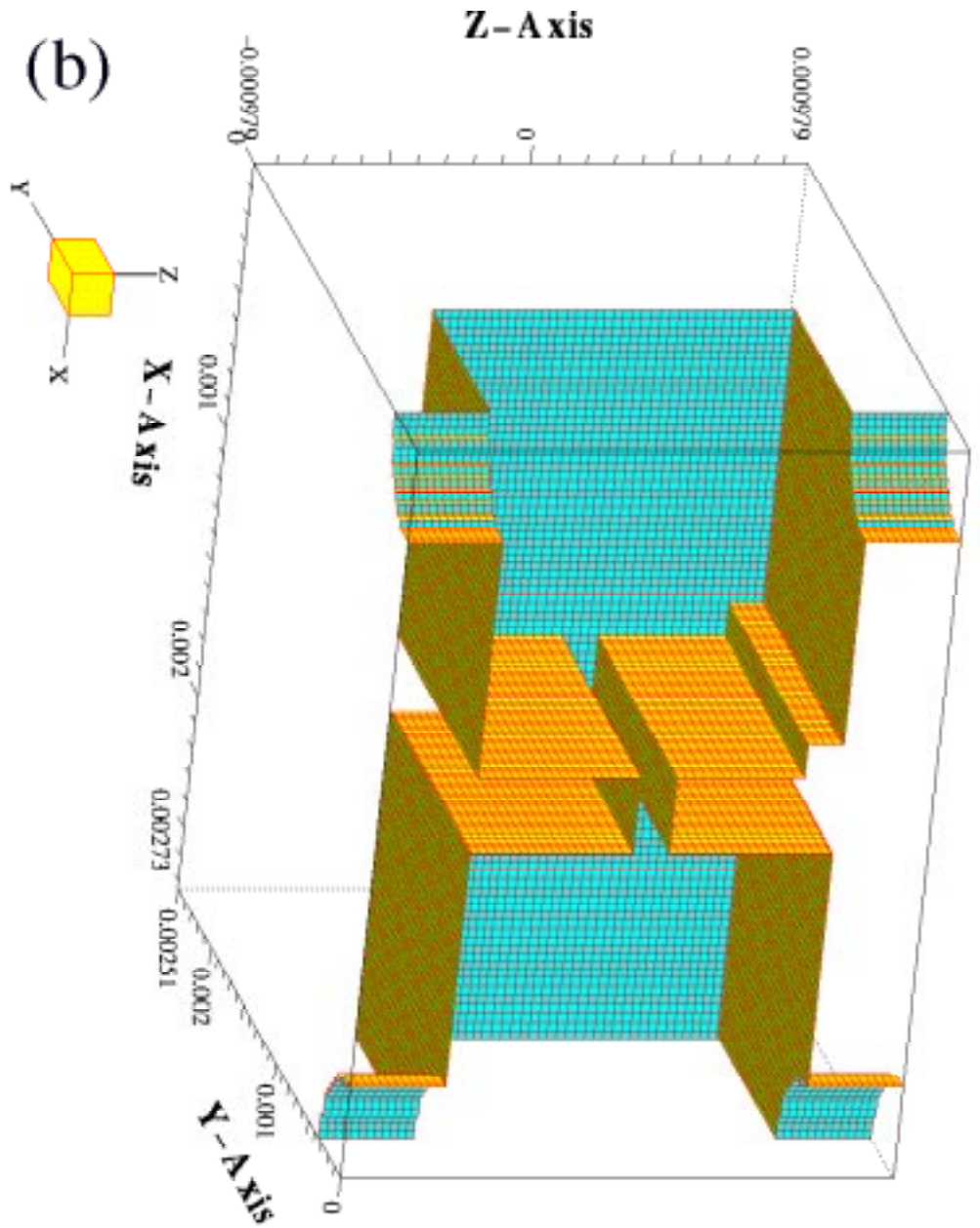
(b)
Z – Axis
-0.000979
0
0.000979
Y
Z
X
X – Axis
0.001
0.002
0.00273
Y – Axis
0.00251
0.002
0.001
0

FIG. 17(b)

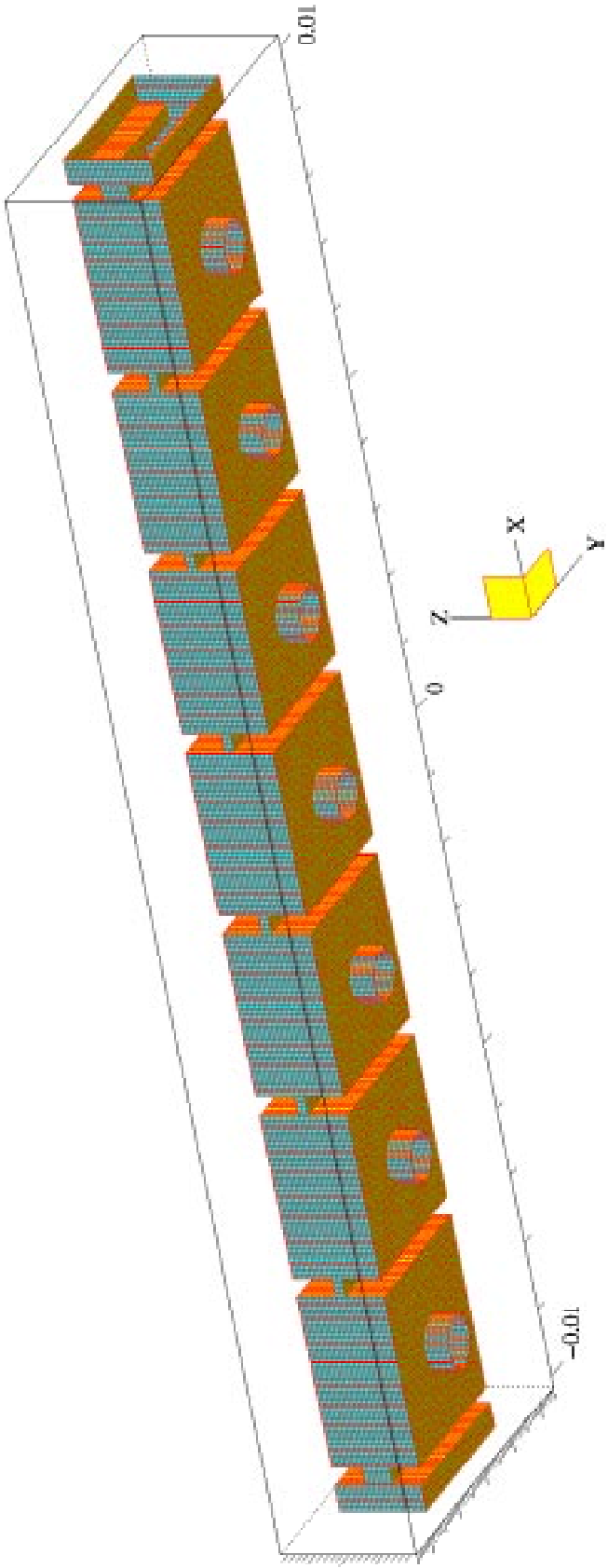


FIG. 18

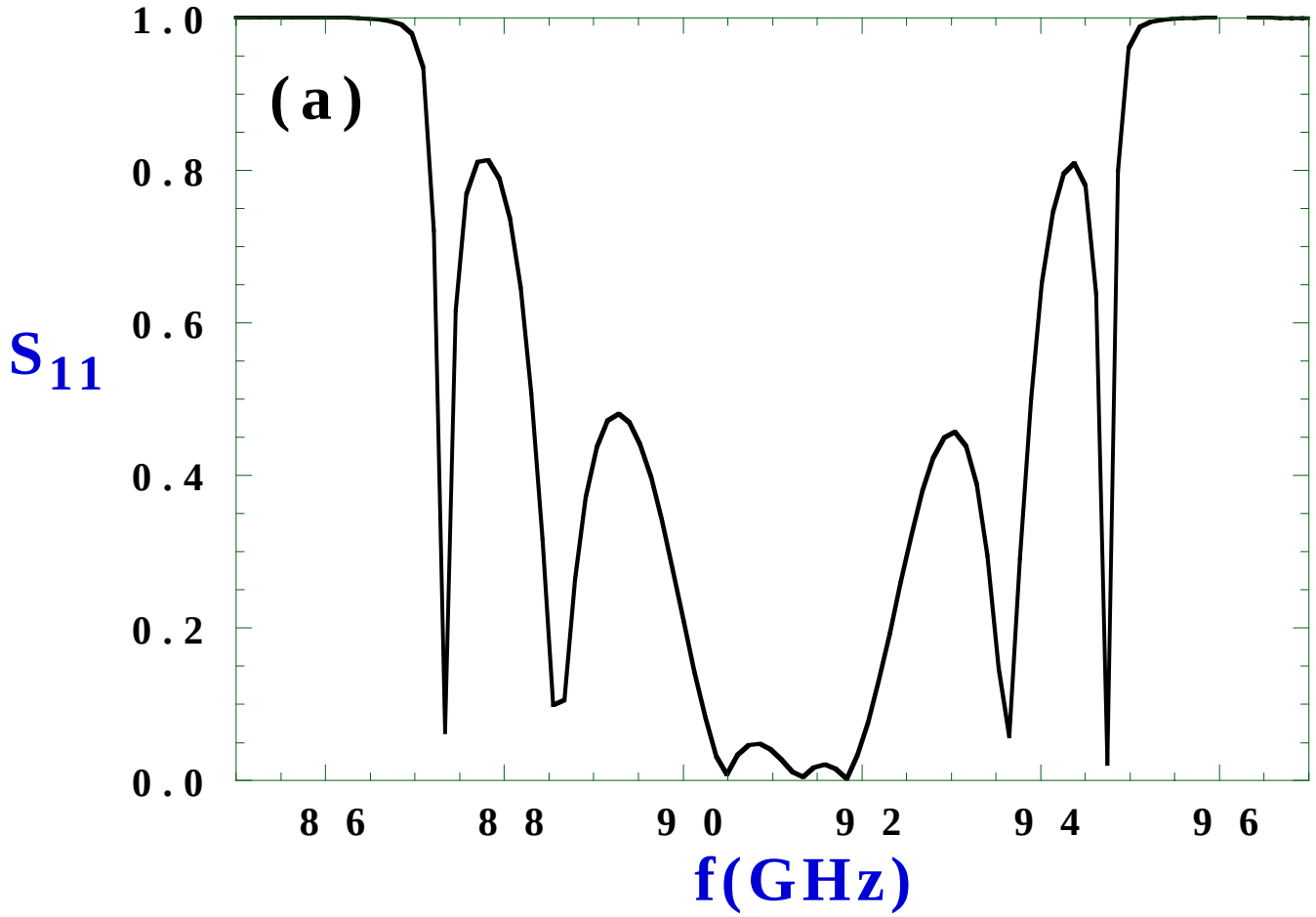


FIG. 19(a)

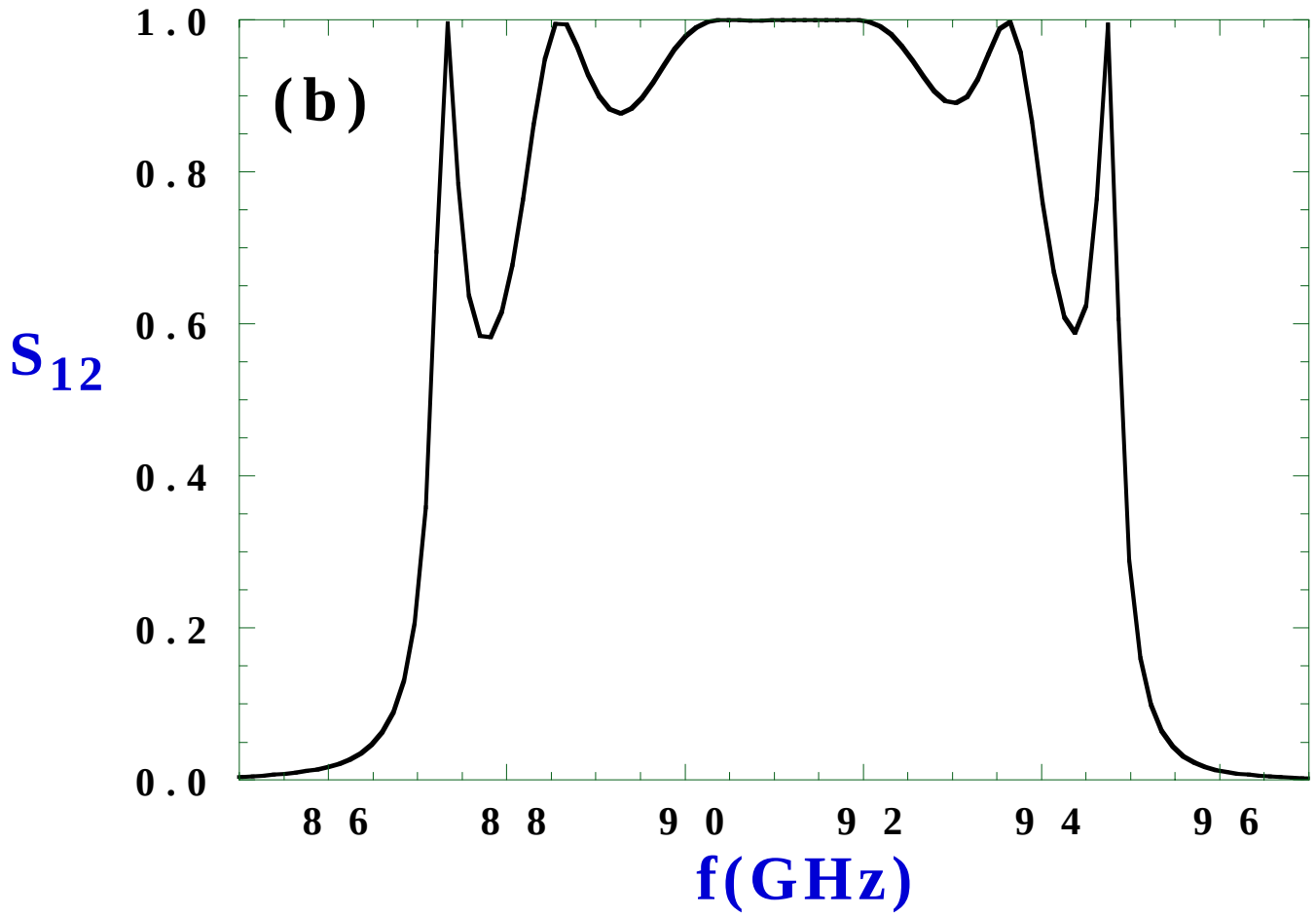


FIG. 19(b)

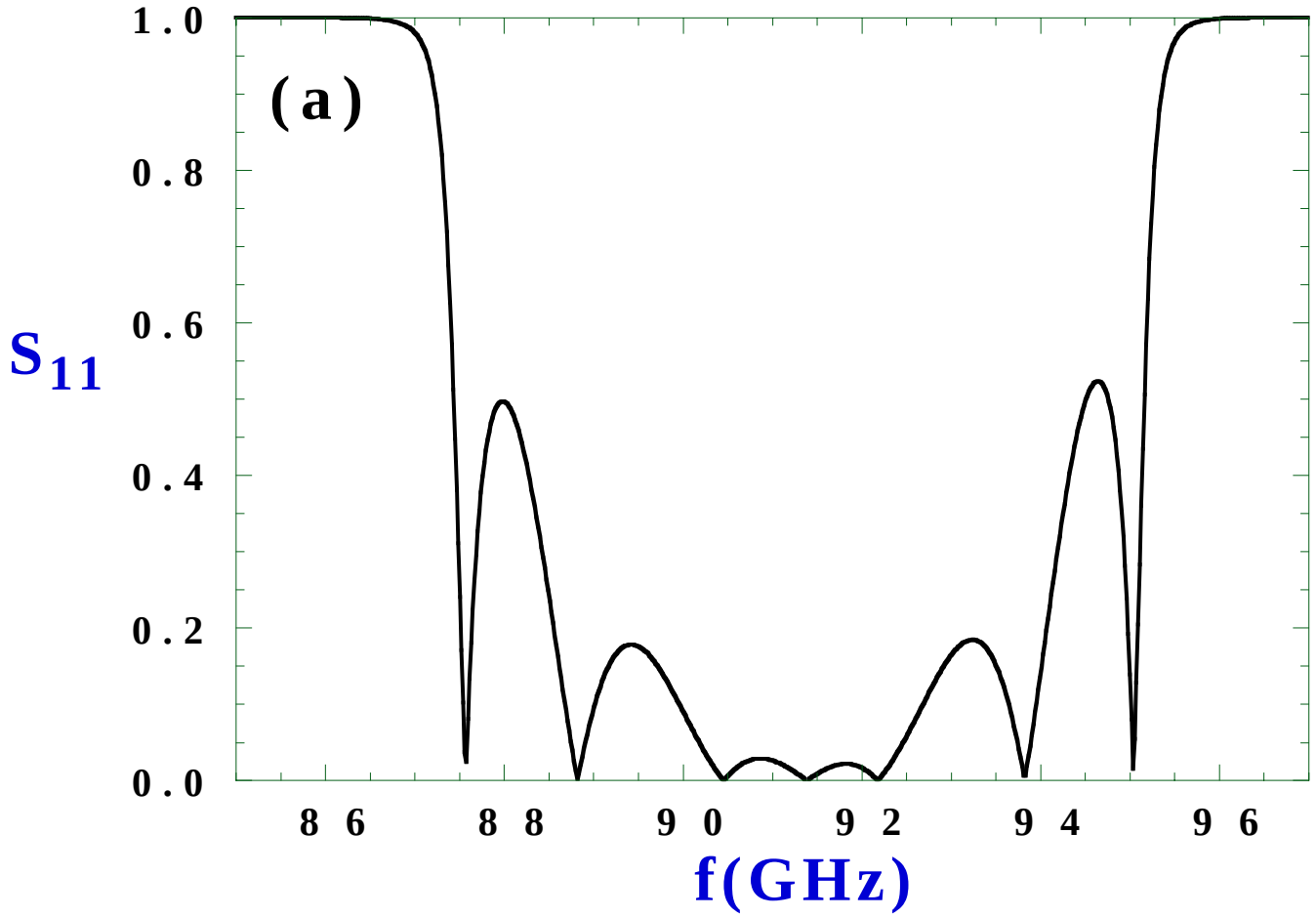


FIG. 20(a)

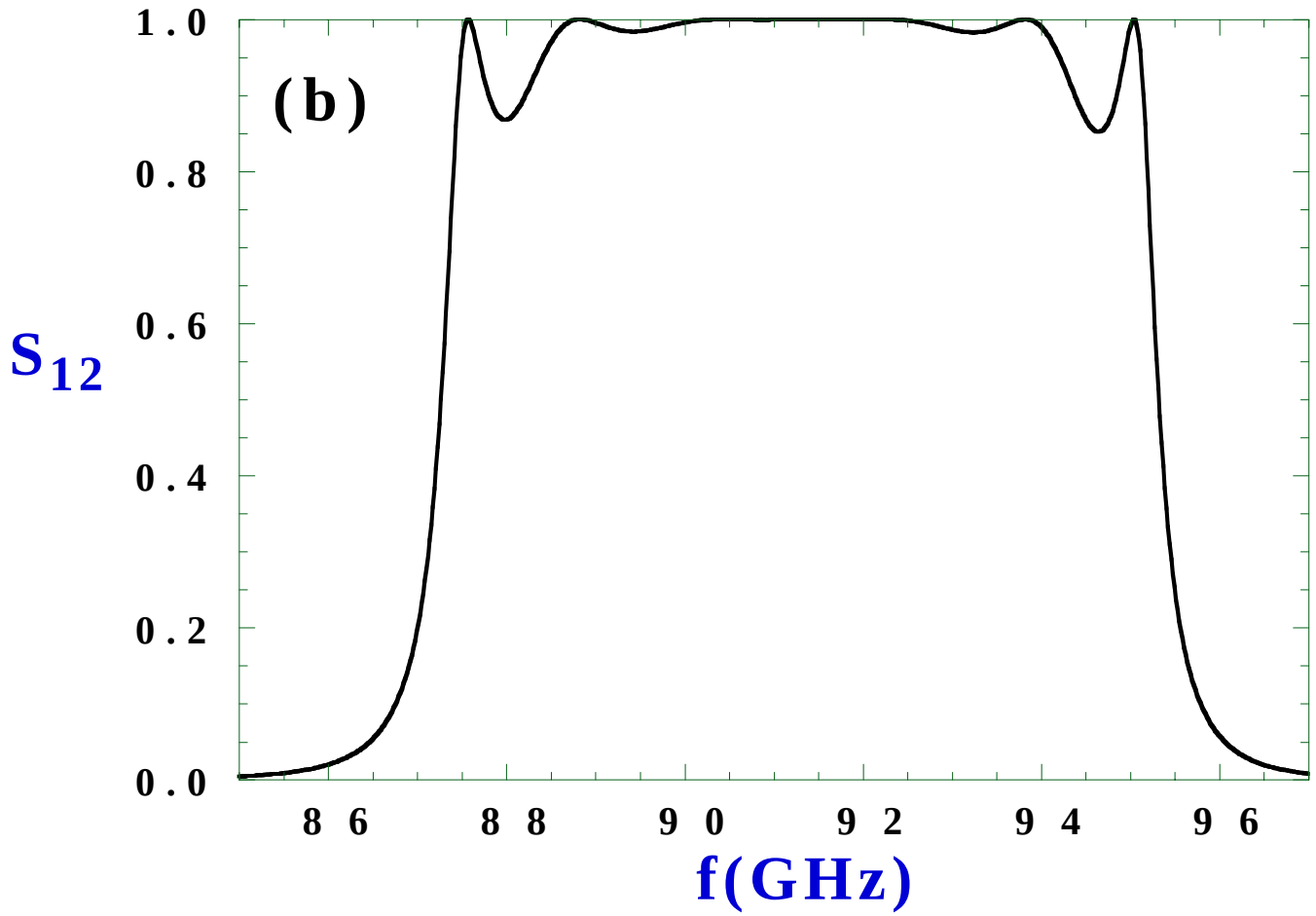


FIG. 20(b)